

AEROTHERMODYNAMIC SHAPE OPTIMIZATION USING
DSMC AND POD-RBF METHODS

A THESIS SUBMITTED TO
THE GRADUATE SCHOOL OF NATURAL AND APPLIED SCIENCES
OF
MIDDLE EAST TECHNICAL UNIVERSITY

BY

HALİT KUTKAN

IN PARTIAL FULFILLMENT OF THE REQUIREMENTS
FOR
THE DEGREE OF MASTER OF SCIENCE
IN
AEROSPACE ENGINEERING

JULY 2018

Approval of the thesis:

**AEROTHERMODYNAMIC SHAPE OPTIMIZATION USING
DSMC AND POD-RBF METHODS**

submitted by **HALİT KUTKAN** in partial fulfillment of the requirements for the degree of **Master of Science in Aerospace Engineering Department, Middle East Technical University** by,

Prof. Dr. Halil Kalıpçılar
Dean, **Graduate School of Natural and Applied Sciences**

Prof. Dr. Ozan Tekinalp
Head of Department, **Aerospace Engineering**

Assoc. Prof. Dr. Sinan Eyi
Supervisor, **Aerospace Engineering Dept., METU**

Examining Committee Members:

Assoc. Prof. Dr. Utku Kanoğlu
Aerospace Engineering Dept., METU

Assoc. Prof. Dr. Sinan Eyi
Aerospace Engineering Dept., METU

Asst. Prof. Dr. Mustafa Perçin
Aerospace Engineering Dept., METU

Asst. Prof. Dr. Sıtkı Uslu
Mechanical Engineering Dept., TOBB ETU

Asst. Prof. Dr. Ali Ruşen Çete
Aerospace Engineering Dept., ADANA BTU

Date: 23.07.2018

I hereby declare that all information in this document has been obtained and presented in accordance with academic rules and ethical conduct. I also declare that, as required by these rules and conduct, I have fully cited and referenced all material and results that are not original to this work.

Name, Last name: Halit KUTKAN
Signature :

ABSTRACT

AEROTHERMODYNAMIC SHAPE OPTIMIZATION USING DSMC AND POD-RBF METHODS

Kutkan, Halit

MS., Aerospace Engineering Department

Supervisor: Assoc. Prof. Dr. Sinan Eyi

June 2018, 72 pages

This thesis study presents a hybrid method based on Proper Orthogonal Decomposition (POD) with Radial Basis Function (RBF), on Direct Simulation Monte Carlo (DSMC) solutions for aerothermodynamic front surface optimization of Stardust re-entry. Gaussian and multiquadric RBFs are implemented for comparison, and multiquadric functions are chosen due to their insensitivity to diverse shape parameters. Cubic uniform B-spline curves are used innovatively for parameterization of the geometry change, instead of curve fitting the geometry itself. This makes possible to reduce the number of design variables. Gradient based optimization strategy is implemented by regarding the distributions of pressure, shear stress and heat flux along the surface of the geometries. DS2V two dimensional axisymmetric DSMC solver is used as the physics solver, and 11 species air model are chosen with 41 chemical reactions according to atmospheric conditions of the re-entry. Different geometries are obtained via deviating the design variables arbitrarily to form a snapshot pool. In this manner, the approximation success of the POD-RBF methodology is tested on highly nonlinear flow conditions with arbitrarily chosen design

of experiment. Finally, the optimized geometries are simulated via DSMC code and the solutions are compared with the solutions of POD-RBF Reduced Order Model (ROM). Method lowered the optimization time extraordinarily and provided satisfactory results.

Keywords: DSMC, POD, RBF, Hypersonic flow, Optimization

ÖZ

DSMC VE POD-RBF YÖNTEMLERİ KULLANARAK AEROTERMODİNAMİK ŞEKİL OPTİMİZASYONU

Kutkan, Halit

Yüksek Lisans, Havacılık ve Uzay Mühendisliği

Tez Yöneticisi: Doç. Dr. Sinan Eyi

Vgo o w l '2018, 72 Sayfa

Bu tez çalışması, Stardust atmosphere giriş aracının aerotermodinamik ön yüzey optimizasyonu için Doğrudan Benzetim Monte Carlo (DSMC) çözümleri üzerinde Radyal Temel Fonksiyonu (RBF) ile Uyumlu Dikayrışım Yöntemine (POD) dayanan bir melez yöntem sunmaktadır. Gauss tipi ve multikvadrik radyal temel fonksiyonları karşılaştırma için uygulanmıştır ve çeşitli şekil parametrelerine duyarsızlıklarından dolayı multikvadrik fonksiyonlar seçilmiştir. Kübik üniform B-spline eğrileri, geometriye eğri uydurmak yerine, geometri değişiminin parametrelendirilmesi için yenilikçi bir şekilde kullanılmıştır. Bu, tasarım değişkenlerinin sayısını azaltmayı mümkün kılar. Gradyan bazlı optimizasyon stratejisi, geometrinin yüzeyi boyunca basınç, kesme gerilmesi ve ısı akısının dağılımları ile gerçekleştirilir. DS2V iki boyutlu aksel simetrik DSMC çözücü, fizik çözücü olarak kullanılır ve 11 tür içeren hava modeli, atmosphere giriş aracının atmosferik koşullarına göre 41 adet kimyasal reaksiyon içeren model ile birlikte kullanılır. İndirgenmiş model için çözüm havuzu, B-spline eğrilerinin parametrelerini rastgele değiştirerek elde edilir. Bu şekilde, POD-RBF metodolojisinin yakınsama başarısı, keyfi olarak seçilen deney tasarımı üzerinde yüksek nonlineerliğe sahip akış koşullarında test edilir. Son olarak, optimize edilmiş geometriler DSMC kodu ile simüle edilir ve çözümler POD-RBF

indirgenmiş modelin çözümleri ile karşılaştırılır. Yöntem, optimizasyon süresini ciddi bir şekilde düşürmüştür ve tatmin edici sonuçlar vermiştir.

Anahtar Kelimeler: Doğrudan Benzetim Monte Carlo Yöntemi, Uyumlu Dikayrışım Yöntemi, Radyal Temel Fonksiyonlar, Hipersonik akış, Optimizasyon

To my family

ACKNOWLEDGEMENTS

I would like to thank my supervisor Assoc. Prof. Dr. Sinan Eyi for his guidance and endless support. He has always stood by me to listen and find solutions for my problems. His endless patience and supports has made me finish my MSc degree.

I would like to thank my former director İbrahim Pamuk for his understandings along my MSc study.

I would like to thank my friend and former colleague Uğur Aydın for his supports in working environment. He has always taken my responsibilities and provided me time to study on my thesis.

I would like to thank my friend Oğuz Kaan Onay for his supports and friendship along the thesis. He has always replied my questions about thesis study, even on by phone.

I would like to thank our department secretary Derya Kaya Topa for her supports in administrative affairs.

I would like to thank my precious family. They have believed in me all the time and supported me.

Finally, I would like to thank my other half Seda Kutkan for her endless patience, support and love since we were.

TABLE OF CONTENTS

ABSTRACT	v
ÖZ	vii
ACKNOWLEDGEMENTS	x
TABLE OF CONTENTS	xi
LIST OF TABLES	xiii
LIST OF FIGURES	xiv
CHAPTERS	
INTRODUCTION	1
1.1. Re-entry Vehicles	1
1.2. Direct Simulation Monte Carlo	1
1.2.1. DS2V DSMC Code	3
1.3. Reduced Order Modeling	5
1.4. DOT Optimization Tool	6
1.5. Aim of the Study	7
MOLECULAR SIMULATION OF HYPERSONIC GAS FLOWS	9
2.1. Governing Equations: Basics of Kinetic Theory	10
2.1.1. Velocity Distribution Function	10
2.1.2. Boltzmann Equation	13
2.1.3. Moment and Conservation Equations	17
2.1.4. Chapman Enskog Expansion	18
2.2. DSMC Procedures	19
GEOMETRY PARAMETERIZATION	23
3.1. Bezier Curves	25
3.2. B-spline Curves	26
3.2.1. B-spline Curve Fitting and Fitting Stardust Capsule	27
3.2.2. B-spline Parameterization of Geometry Change.....	29
REDUCED ORDER MODELING	33
4.1. Proper Orthogonal Decomposition.....	34
4.1.1. POD Snapshots	35
4.1.2. POD SVD.....	37

4.2.	Radial Basis Functions.....	38
4.3.	POD-RBF ROM Model Development	40
4.3.1.	Comparison of RBFs	42
	GRADIENT BASED OPTIMIZATION	45
5.1.	Optimization Procedure	46
	RESULTS AND DISCUSSION.....	49
6.1.	DSMC Flow Simulation Validation	49
6.1.1.	Simulation Conditions	49
6.1.2.	Validation of Simulation	51
6.2.	Optimization Results.....	52
6.2.1.	Optimized Geometry Solutions Validation	53
6.2.2.	Comparison of Stardust and Optimized Geometries	59
	CONCLUSION	67
	REFERENCES	69

LIST OF TABLES

TABLES

Table 1 Freestream conditions at 81 km altitude	49
Table 2 List of chemical reactions	50
Table 3 Validation of case 1 maximizing drag on tabulated results (Opt. Geom. 1)	54
Table 4 Validation of case 2 minimizing heat energy on tabulated results (Opt. Geom. 2).....	55
Table 5 Validation of case 3 minimizing maximum heat flux on tabulated results (Opt. Geom. 3)	57
Table 6 Validation of case 4 maximizing volume on tabulated results (Opt. Geom. 4)	58
Table 7 Tabulated results of Stardust and Opt. geom. 1	60
Table 8 Tabulated results of Stardust and Opt. geom. 2	63
Table 9 Tabulated results of Stardust and Opt. geom. 3	64

LIST OF FIGURES

FIGURES

Figure 1 Application feasibility of numerical methods	2
Figure 2 Interactive graphical user interface of DS2V program	4
Figure 3 Typical set of initial sampling cells	4
Figure 4 Adapted sampling cells	5
Figure 5 Adapted collision cells	5
Figure 6 DOT Optimization tool working principle	7
Figure 7 Typical molecule and element in velocity space	10
Figure 8 Molecular flux to and from a phase space element $d\mathbf{c}d\mathbf{r}$	14
Figure 9 Effective volume swept by the test molecule amongst the stationary field molecules	15
Figure 10 Comparison of flow behaviour of sharp and blunt vehicles in supersonic and hypersonic flow	24
Figure 11 Schematic representation of re-entry capsule	24
Figure 12 Stardust geometrical dimensions	28
Figure 13 B-spline curve fitting of Stardust geometry	29
Figure 14 Control polygons and individual B-spline curves for two different geometries.....	30
Figure 15 Base and resulting geometries.....	30
Figure 16 Forming POD data matrix.....	36
Figure 17 Error charts of multiquadric and Gaussian RBFs on sample 45 and sample 75 extrapolation.....	43
Figure 18 Optimization scheme.....	47
Figure 19 Contour plots of Stardust	51
Figure 20 Comparison of pressure and heat flux distributions	51
Figure 21 Case 1 maximizing drag optimization results validation (Opt. geom. 1)	53
Figure 22 Case 2 minimizing heat energy optimization results validation (Opt. Geom. 2).....	55

Figure 23 Case 3 minimizing maximum heat flux optimization results validation (Opt. Geom. 3)	57
Figure 24 Case 4 maximizing volume optimization results validation (Opt. Geom. 4)	58
Figure 25 Comparison of Stardust and Opt. geom. 1.....	60
Figure 26 Comparison of Stardust and Opt. geom. 2.....	62
Figure 27 Comparison of Stardust and Opt. geom. 3.....	64

CHAPTER 1

INTRODUCTION

1.1. Re-entry Vehicles

Re-entry vehicles are the most common type of hypersonic vehicles. They enter atmosphere at high altitudes where the air is highly rarefied. They are designed for slowing down the velocity by increasing the drag force along their trajectory. However, they are exposed to very high velocities where the highly energetic thermochemical effects are dominant. In addition to this, strong shock waves generate tremendous heat on the windward side. Hence, the design requires accurate prediction of surface quantities such as heat flux, pressure and shear stress to calculate the aerodynamic forces and moments. These properties are not only responsible for the aerodynamic performance of the vehicle, they are also responsible for the selection and the sizing of the thermal protection system (TPS), which protects the vehicle from extreme heating. In this manner, designs of the re-entries need to be optimized.

1.2. Direct Simulation Monte Carlo

DSMC method is a particle-based stochastic approach which physically simulates the behaviour of gas molecules in the flow field. It is derived from the Boltzmann Equation through Chapman Enskog approximation and the details of the method can be found from [1]. It was developed by G.A. Bird in the late 1960's and became popular in the field of aerospace due to its accuracy on rarefied gas flows with high Knudsen number [2].

$$Kn = \frac{\lambda}{D} \quad (1)$$

Knudsen number, Kn is defined as the ratio of mean free path, λ to characteristic dimension, D of the flow field. In such conditions mean free path between the gas molecules are quite high to consider the stream as continuous medium (Fig. 1).

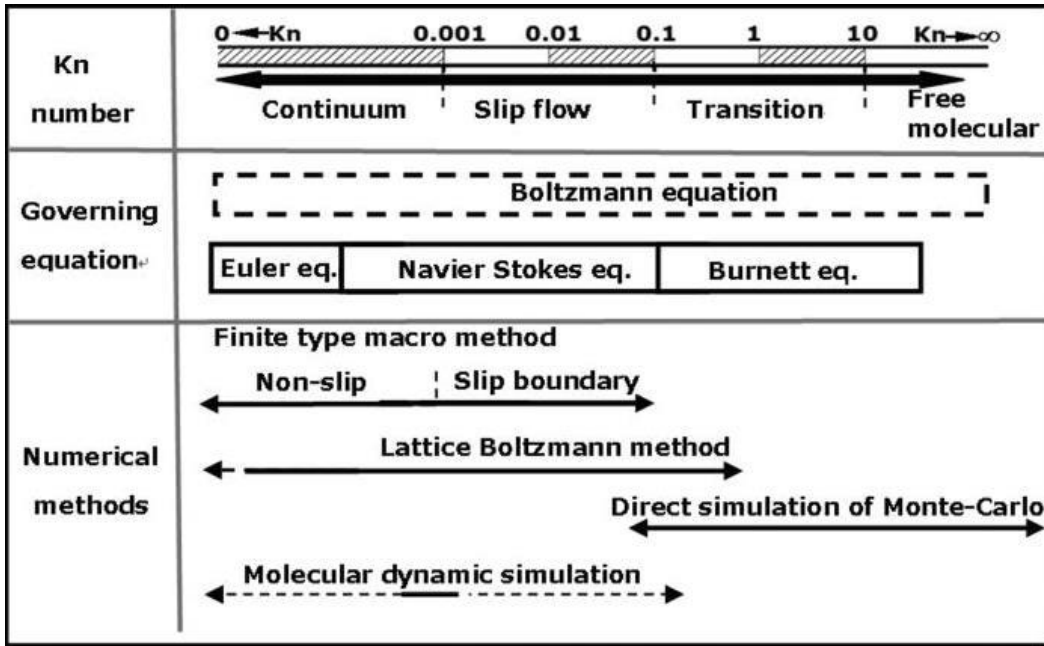


Figure 1 Application feasibility of numerical methods [3]

According to the values of Kn , the flow regime can be classified in terms of continuum, slip, transition and free molecule. Continuum flow refers the regime where the Navier-Stokes equations are completely valid. Opposingly, free molecule regime is the regime with no intermolecular collisions. Slip regime can be assumed as similar to continuum regime except of its velocity slip and temperature jump conditions at solid surfaces. And the transition regime is the regime that lies between the slip and the free molecular regime [4].

According to Fig. 1, for the values of Kn , bigger than 0.1, DSMC is the only feasible numerical method, and this range can be widened up to 0.001, depending on the local Knudsen number. Depending on the arbitrary choice of the

characteristic length, these classifications may lead to miscarriages while defining the regime of the flow. Additionally, any single flow may contain more than one flow regime so that the treatment of local Kn rather than overall one comes into prominence.

Paying attention to the applicability of the Boltzmann equation and remembering the origin of the method, molecular dynamic simulation (MD) and the direct simulation monte carlo (DSMC) are valid in all of the regimes if the required computation expense is satisfied. Likewise, the simplest form of DSMC gives the solution to Boltzmann equation when the number of particles goes to infinity while the grid size and time step are going to zero [4].

1.2.1. DS2V DSMC Code

DS2V is two dimensional DSMC program developed by G.A. Bird. It has been used in many times in its field and can be regarded as commercial quality program [4]. It has an interactive graphical user interface (Fig. 2), and the source code is available. In other words, one can modify the code in terms of implementations of newer models or for any other goal. The code is capable of simulating gas flows in two-dimensional plane and axisymmetric conditions.

The program reads data from an input file, and this file can be formed by manually or via the graphical user interface. It has predefined air models and chemical reaction sets, so the implementations of the flow conditions are easy. The total number of molecules in the simulation are entered to the program by defining the size of memory allocation. According to this, program calculates the number of molecules and also divides the flow field into the grids. However, the number of molecules and the cells can be expanded by the user in terms of entering a multiplication factor and adapting the grid respectively.

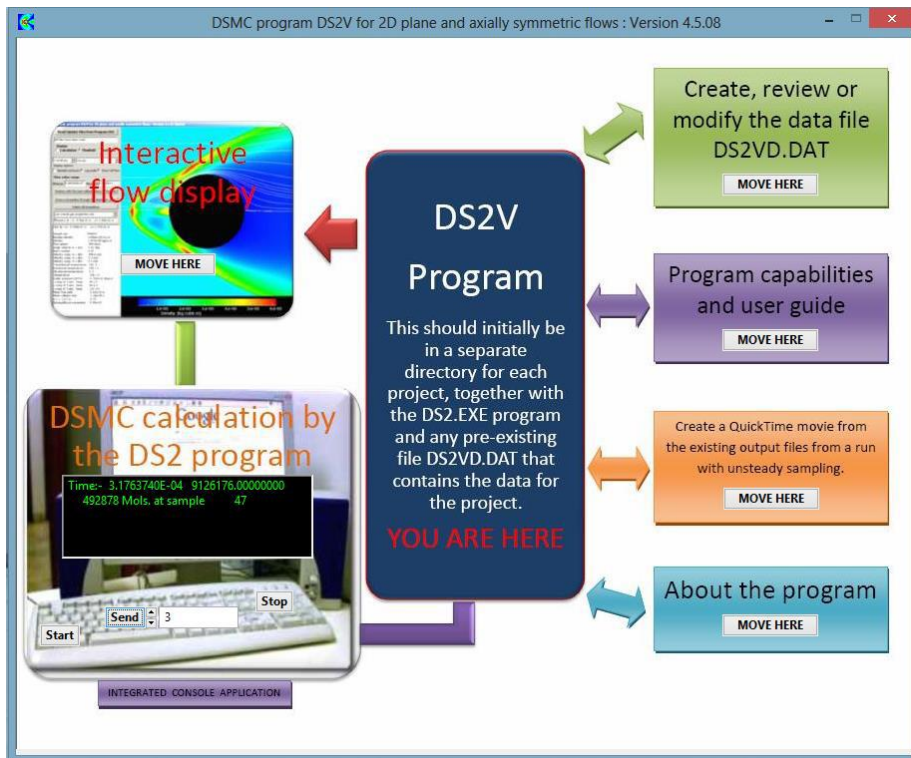


Figure 2 Interactive graphical user interface of DS2V program [4]

DSMC requires two sets of grids for sampling and collision processes and the grid adaption is made by defining the maximum number of molecules in each sampling and collision cells. In the figures below (Fig. 3, 4 and 5) initial sampling cells, adapted sampling cells and the adapted collision cells are shown.

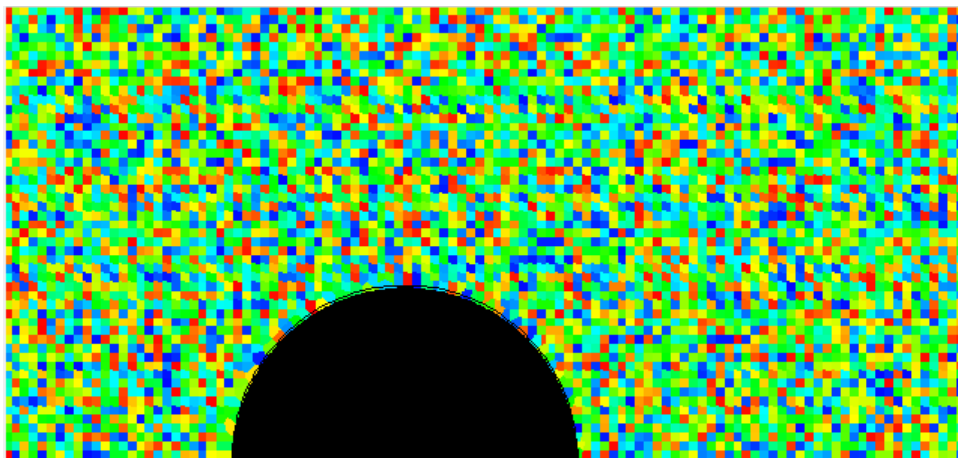


Figure 3 Typical set of initial sampling cells [4]

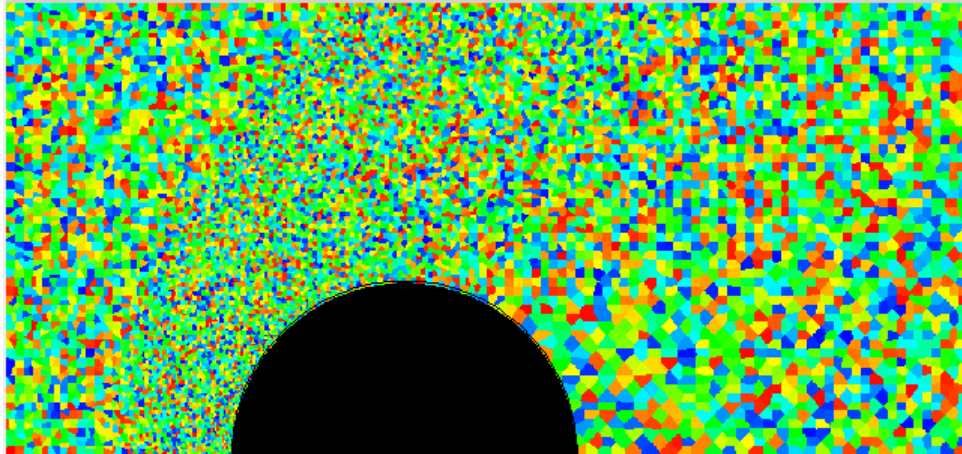


Figure 4 Adapted sampling cells [4]

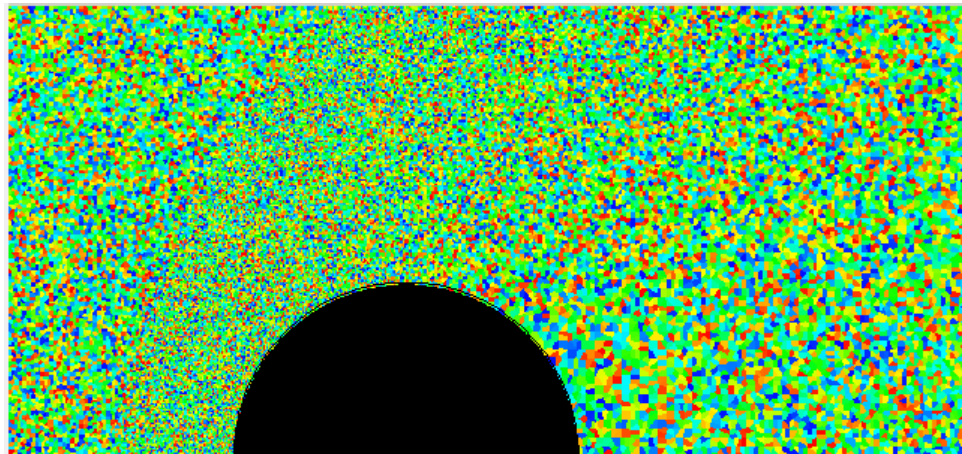


Figure 5 Adapted collision cells [4]

1.3. Reduced Order Modeling

DSMC method is very useful while simulating rarefied gas flows. However, its utilization for optimization study still needs a considerable amount of computation process. To reduce the computation time and dynamize the optimization process, Reduced Order Modeling techniques may be used. These techniques provide a low dimensional approximation for the full high dimensional system by reflecting the dominant characteristics [5].

Amongst the other ROM techniques Proper Orthogonal Decomposition technique stands out by its extensive usage in the field of aerodynamics. POD is such a mathematical method that provides an optimally ordered orthonormal basis in the least squares sense for a given set of data [5]. POD can obtain this orthonormal basis either taking singular value decomposition (SVD) of the original data matrix or determining the eigenvector matrix of the covariance matrix. Furthermore, this basis can be used either for reconstruction or extrapolation of the prospective vectors.

POD has been widely used in the field of aerodynamics with linear regression models [6]–[9] successfully. However, its usage with linear regression models fails down when the nonlinear flow conditions are dominant. Jing [10] investigated the interpolation and extrapolation capability of POD on NACA 0012 airfoil in transonic conditions with linear regression model and showed the inaccuracy in extrapolation. The reason for this, lies under the evaluation of coefficients of POD basis modes. Linear regression method like least squares cannot extract the nonlinear system behaviour and may cause fallacies especially in the flows where the discontinuities occur. To overcome this situation, nonlinear regression methods such as: quadratic polynomials or neural networks like radial basis functions (RBF) may have been utilized. Having said that, the nonlinear regression examples in the literature have been applied on the continuum approach solutions such as: FEM or CFD [11]–[17]. In this sense, the present study may have a place in the literature, for investigating the success of POD with nonlinear regression on particle based stochastic approach solutions.

1.4. DOT Optimization Tool

DOT is such a general-purpose gradient based commercial optimization tool that is provided as software libraries [18]. It provides the optimization algorithm and users must provide the main program and evaluation subroutines. Evaluation subroutines are prepared as the functions of design variables and main program manages the linkage between DOT and the evaluation subroutines (Fig. 6).

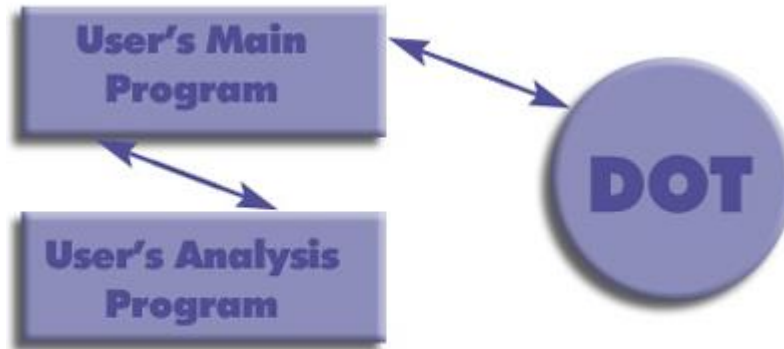


Figure 6 DOT Optimization tool working principle [18]

User's main program must provide the setup of the optimization. In other words, number of design variables, defining side constraints, selection of optimization type and etc must be specified in the main program. Secondly, user's analysis program must provide the objective and constraint functions and according to the optimization, it must also provide the gradient information.

Optimization process starts with calling DOT from main program. Then DOT changes the values of design variables in order to find the optimum. Afterwards, it turns back to main program with new design variables. Main program transfers these new variables to analysis program. Analysis program calculates the objective and constraint functions and send them to the main program and main program transfers these values to DOT to obtain the new values of design variables. And this routine is continued till the optimum design point is reached.

1.5. Aim of the Study

In the present study, aerothermodynamic front shape optimization of the Stardust re-entry has been aimed. Innovative parameterization approach has been made via implementing the B-spline curves on the geometry change, instead of fitting the geometry itself. Thus, the number of control points has been able to be decreased.

The base Stardust geometry had been composed of 600 intervals and the intervals of the cubic B-splines were also held as equal. Various geometries were obtained by summing up the cubic B-spline's interval nodes and the base Stardust geometry nodes. DS2V direct simulation monte carlo code [4] was used as the physics solver and POD-RBF code was developed for model order reduction.

Sampling space had been composed of 40 arbitrarily chosen geometry solutions initially and it was expanded up to 90 solutions finally. Leave-One-Out (LOO) cross validation method [17] was implemented for specifying these requirements. Multiquadric and gaussian RBFs were implemented for comparison, and multiquadric RBFs was chosen for optimization in case of its relative insensitivity to model parameter. Gradient based optimization tool DOT [19] was used for optimization and four different optimized geometry were obtained at the end of the optimization by changing the objective and the constraint functions.

Developed POD-RBF code was used as the solver of optimization. Pressure, shear stress and heat flux distributions were obtained as corresponding outputs from POD-RBF code to the inputs of various geometries' parameters. Aerodynamic drag and the total heat energy were calculated by integrating the distribution of pressure, shear stress and heat flux along the surface of the geometries. The optimized geometries were simulated via DS2V after the optimization. Pressure, shear stress and heat flux distributions were plotted and compared with the solutions of reduced order model.

CHAPTER 2

MOLECULAR SIMULATION OF HYPERSONIC GAS FLOWS

Molecular approach treats the gases as discrete particles. Unlike the macroscopic models, the flow properties like velocity, density, pressure and temperature are not dependent variables. It provides information of positions, velocities and states of particles in every time step. Being different than macroscopic approach, the fundamental equation at this level is Boltzmann equation. This makes possible the molecules are in their positions with having only dependent variables as their states. However, according to the physics of the flow they can have number of independent variables.

The monatomic gas with no internal degrees of freedom can be given as an example to the simplest case. Despite this, the simulated particles have additional three velocity components at the phase space. In other words, any one-dimensional steady flow becomes a three-dimensional and any two-dimensional flow becomes a five-dimensional flow [1] in the phase space. This is sourced by treating the velocities of any particle in three-dimensional as being independent of the dimension of the flow. This makes the analytical solution of Boltzmann equation is impossible and leads to difficulties in numerical modelling. Nevertheless, the discrete structure of gas gives opportunity to physical simulation of particles rather than developing mathematical or numerical model.

2.1. Governing Equations: Basics of Kinetic Theory

2.1.1. Velocity Distribution Function

In real gas flows at molecular level, the complete description of the flow requires the position, velocity and state information of all particles in the flow field in any time step [1]. However, having such information is impossible in real life. Therefore, the usage of statistical distribution functions would be beneficial.

Considering homogeneous gas in a physical space with total N number of molecules. Any molecule with velocity c , and velocity components u , v , w can be defined as a point in the velocity space (Fig. 7), and just like the x , y , z in cartesian coordinates in the physical space, u , v , w refers to the axis of velocity space.

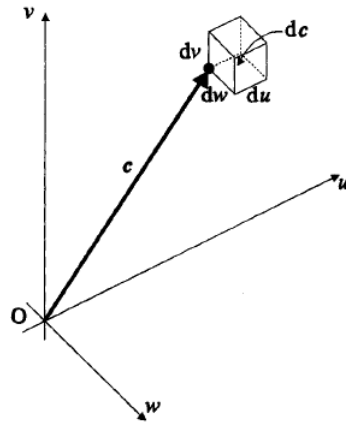


Figure 7 Typical molecule and element in velocity space [1]

Then the velocity distribution function, f can be defined as follows:

$$\frac{dN}{N} = f du dv dw \quad (2)$$

or

$$\frac{dN}{N} = fdc \quad (3)$$

where dN denotes the number of molecules whose velocity components are in the range of u to $u+du$, v to $v+dv$ and w to $w+dw$. Thus, the product $dc = dudvdw$ is entitled as the volume element in the velocity space.

Since the distribution function is normalized function, its integration over the velocity space will be equal to one.

$$\int_{-\infty}^{\infty} \int_{-\infty}^{\infty} \int_{-\infty}^{\infty} f dudvdw = \int_{-\infty}^{\infty} fdc = \frac{N}{N} = 1 \quad (4)$$

Calculation of macroscopic properties requires a relation with the distribution function. Considering Q referring to any of the molecular quantity, the macroscopic correspondence can be calculated via averaging. Then the mean value can be expressed as follows:

$$\bar{Q} = \int_{-\infty}^{\infty} Qfdc \quad (5)$$

Similarly, the stream velocity can be summarized as follows:

$$\bar{c} = \int_{-\infty}^{\infty} cfdc \quad (6)$$

Introducing r and dr as the position vector and volume element in physical space and t as time, the product $dcdt$ is denoted as volume element in phase space. And phase space can be imagined as the combination of velocity and physical spaces. Then the single particle distribution function $F(c,r,t)$ in phase space can be evaluated as follows:

$$dN = F(c, r, t)dcdr \quad (7)$$

By the way, dN now refers to the number of molecules in the phase space element $dcdr$. In cartesian coordinates dN gives the number of molecules with velocities ranging from u to $u+du$, v to $v+dv$ and w to $w+dw$ and with positions x to $x+dx$, y to $y+dy$ and z to $z+dz$. And $dcdr$ becomes $dudvdwdxdydz$ in cartesian coordinates. Being different than f , F refers to integer number rather than fraction of molecules in the phase space element. So, the integration of F over the phase space gives the total number of molecules in the system.

By equalizing the Eqns. (3 and 7) we obtain the equation below:

$$dN = Nfdc = F(c, r, t)dcdr \quad (8)$$

It is important to pay attention to Eqn. 8 that, N refers to the number of molecules in physical space volume element dr and dN refers to the number of molecules in the phase space volume element $dcdr$.

Introducing new variable n as the number density in physical space element as N/dr and similarly number density in phase space element will be $dN/dcdr$. So that, the Eqn. 8 turns into the form below:

$$\frac{dN}{dcdr} = nf = F(c, r, t) \quad (9)$$

Paying attention to Eqn. 9, f depends on both r and t . The presence probability of molecule number 1 in a phase space volume element dc_1dr_1 at time t is $F^{(1)}(c_1, r_1, t)$ and it is independent from the positions of other $N-1$ number of molecules. And the number of molecules in the phase space element at that time can be evaluated by multiplying the total number of molecules N with the probability $F^{(1)}$ of molecule.

On the other hand, the presence probability of two molecules in a phase space element can be found by the product of the two molecules' probabilities and can be expressed as follows:

$$F^{(2)}(c_1, r_1, c_2, r_2, t) = F^{(1)}(c_1, r_1, t)F^{(1)}(c_2, r_2, t) \quad (10)$$

Because of the indistinguishability of the molecules, the probability functions of each molecule are the same. This is why the right-hand side of the Eqn. 10 are written as the multiplication of $F^{(1)}(\dots)F^{(1)}(\dots)$ instead of $F^{(1)}(\dots)F^{(2)}(\dots)$. This approach is entitled as molecular chaos.

Depending on the diatomic or polyatomic structure of molecules, the phase space dimension is expanded upon the internal degrees of freedom. Furthermore, different species require different distribution functions in the gas mixture. Generally, the phase space dimension is specified with the minimum number which is enough for defining the position, velocity, orientation and internal state of molecule.

2.1.2. Boltzmann Equation

At any certain time, the total molecule number in a phase space element can be evaluated via Eqn. 8, and according to Eqn. 9 this expression is also written as $nf dcd r$. Assuming invariance of shape and location of the phase space element along the time, the rate of change of the number of molecules in the element can be expressed as below:

$$\frac{\partial}{\partial t}(nf) dcd r \quad (11)$$

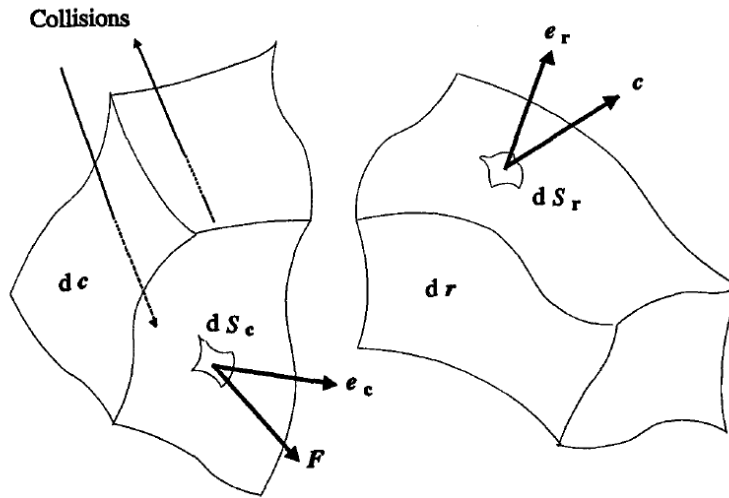


Figure 8 Molecular flux to and from a phase space element $dcd r$ [1]

Fig. 8 may be well understood by analysing the processes which contributes the molecule number change in the phase space element. The phase space element $dcd r$ is expressed as separated into velocity dc and physical space elements dr . This is done because c and r are treated as independent variables. Velocity c is assumed as constant in physical space element dr , and velocity space element dc is assumed as located at the point defined by position vector r .

Fig. 8 explains three processes such as: convection of molecules due to their velocities c , convection of molecules due to external force F and scattering of molecules due to intermolecular collisions. With the dilute gas assumption, collided molecules do not change their locations in physical space, while they are changing their velocities. In other words, they can jump from one to another place in velocity space, however, they remain their positions in physical space. This is why the collisions are shown only at the velocity space element, dc . Another important property of the dilute gas assumption is treating the collisions as binary collisions.

Considering the convection of molecules by the effect of c across the face of dr , and knowing the number of molecules in the phase space element as $nf dcd r$, the

inflow of molecules with velocities c to $c+\Delta c$ across the surface of dr can be written as below [1]:

$$-c \frac{\partial(nf)}{\partial r} dc dr \quad (12)$$

Similarly, the inflow of molecules due to external force, F across the surface of dc can be written also:

$$-F \frac{\partial(nf)}{\partial c} dc dr \quad (13)$$

Let's consider that the collision between a molecule whose velocity is in the range of c to $c+\Delta c$ and a molecule with velocity in the range of c_1 to $c_1+\Delta c_1$ and assuming their post collision velocities as c^* and c_1^* respectively. In this manner, maybe the first molecule is chosen as test molecule and c_r speed may be assigned on it. In this way we assume that the second molecule's speed as zero or the second molecule is stationary.

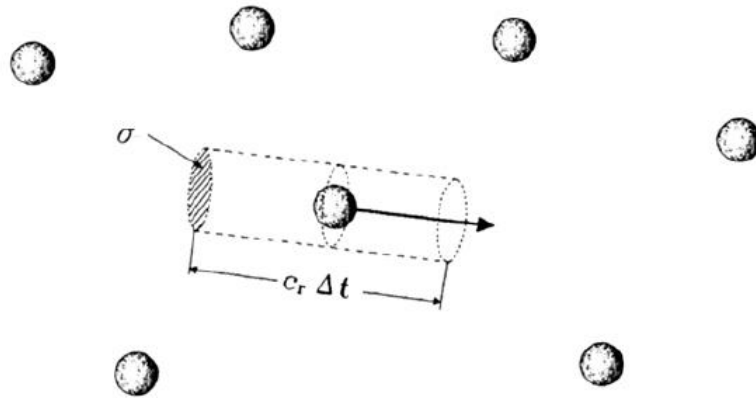


Figure 9 Effective volume swept by the test molecule amongst the stationary field molecules [1]

Then the assigned velocity to test molecule will be $c_r = c - c_1$. And selecting the time interval, Δt is much shorter than the mean collision time, the test molecule

may collide any of the field molecule (with speed c_l to $c_l + \Delta c_l$) within the cylinder of volume $\sigma c_r \Delta t$ as shown in Fig. 9. And using differential time, $d\Omega$ rather than discrete time interval, then the swept volume will be $\sigma c_r d\Omega$ and the increment rate of molecules due to collision scattering will be in the form below:

$$\int_{-\infty}^{\infty} \int_0^{4\pi} n^2 (f^* f_1^* - f f_1) \sigma c_r d\Omega dc_1 dcdr \quad (14)$$

Regarding collision process (Eqn. 14) as responsible for all of the changes in the number of molecules (Eqn. 11, 12 and 13), summing up the changes, equalizing with the collision expression (Eqn. 14) and dividing by $dcdr$ gives the Boltzmann Equation (Eqn. 15) for the simple dilute gas.

$$\begin{aligned} \frac{\partial}{\partial t}(nf) + c \frac{\partial(nf)}{\partial r} + F \frac{\partial(nf)}{\partial c} \\ = \int_{-\infty}^{\infty} \int_0^{4\pi} n^2 (f^* f_1^* - f f_1) \sigma c_r d\Omega dc_1 \end{aligned} \quad (15)$$

If we want to write the Boltzmann Equation for particular species p and q in a mixture of gases, then the equation will be in the form of below:

$$\begin{aligned} \frac{\partial}{\partial t}(n_p f_p) + c_p \frac{\partial(n_p f_p)}{\partial r} + F \frac{\partial(n_p f_p)}{\partial c} \\ = \sum_{q=1}^s \int_{-\infty}^{\infty} \int_0^{4\pi} n_p n_q (f_p^* f_{1q}^* - f_p f_{1q}) \sigma_{pq} c_{rpq} d\Omega dc_{1q} \end{aligned} \quad (16)$$

As stated previously, presence of diatomic or polyatomic molecules (presence of internal degrees of freedom) requires an extended distribution functions which allow the additional dimensions in phase space. Besides, σ collisional cross section is not a constant variable for asymmetric molecules and it varies according to the rotation of molecule [1]. Through the reasons above, the Eqn. 16 is entitled as Generalized Boltzmann Equation.

In Boltzmann (Eqn. 15) or the Generalized Boltzmann Equation (Eqn. 16), the first term on the left-hand side refers to the rate change of molecules along the time, the second term refers to the diffusion of molecules and third term refers to the rate change of molecules due to external force. The term on the right-hand side refers to collision of particles, and if the flow contains chemical reactions, they are treated in this term.

Due to spherically symmetric behaviour of velocity distribution function homogeneous gas can be treated as one dimensional in phase space for Boltzmann solution. However, any physically one-dimensional gas flow becomes three dimensional. Because in this case the velocity distribution function will be axisymmetric instead of spherically symmetric. On the other hand, the velocity distribution function is not axis-symmetric or spherically symmetric in the velocity space in physically two and three-dimensional flows, so it must be treated in three dimensions. Consequently, they become into five and six dimensional flows in the phase space. In addition to these, the time is also added to the flow as an extra dimension.

In accordance with the explanations above, analytical solution of Boltzmann equation is impossible in complex flow problems [1]. And numerical solutions require mesh structure to address the molecules' positions and for easiness in bounding the control volume.

2.1.3. Moment and Conservation Equations

Considering Q as any molecular quantity of single molecule, as it was done in the Eqn. 5, this quantity can be multiplied with the Boltzmann equation and if the resulting equation (Eqn. 17) is integrated over the velocity space, moment of Boltzmann equation is obtained. Thus, the macroscopic properties of monatomic gas can be evaluated.

$$\begin{aligned}
Q \frac{\partial}{\partial t}(nf) + Qc \frac{\partial(nf)}{\partial r} + QF \frac{\partial(nf)}{\partial c} \\
= Q \int_{-\infty}^{\infty} \int_0^{4\pi} n^2 (f^* f_1^* - f f_1) \sigma c_r d\Omega dc_1
\end{aligned} \tag{17}$$

Because of being dependent variables, in the Eqn. 17, Q can be taken into the derivative for the first and the third term on the left-hand side, and Qc can be taken into derivative for the second term. Furthermore, Q can be taken into the integral on the right-hand side. If the terms are integrated over the velocity space and then are summed up, the moment equation of Q , can be written:

$$\frac{\partial}{\partial t}(n\bar{Q}) + \nabla(nc\bar{Q}) - nF \frac{\partial\bar{Q}}{\partial c} = \Delta[Q] \tag{18}$$

Eqn. 18 is entitled as transfer equation or the equation of change, and by replacing the quantity Q , to molecular mass m , molecular momentum mc and molecular kinetic energy $\frac{1}{2}mc^2$, conservation equations of gas dynamics are obtained [1]. The term on the right-hand side of the Eqn. 18 is called as collision integral. According to elastic binary collision mechanics, the total mass, total momentum and the total energy is conserved during the collision process. This means that the collision integral term $\Delta[Q]$ equals to zero, or in other words $[Q]$ remains constant. Thus, the replacement of Q with m gives the conservation of mass, the replacement of Q with mc gives the conservation of momentum and the replacement of Q with $\frac{1}{2}mc^2$ gives the conservation of energy equations.

2.1.4. Chapman Enskog Expansion

Boltzmann equation can be solved for basic cases if the gas is at equilibrium state ($f = f_0$) [20]. On the other hand, if the nonequilibrium conditions are present, the solution becomes impossible. In this manner, Chapman Enskog theory provides a solution to the Boltzmann equation in terms of small disturbance theory. Under

assumption of the small perturbations to the equilibrium state can be defined via the expression below:

$$f = f_0(1 + \varphi_1 + \varphi_2 + \dots) \quad (19)$$

Equilibrium state of gas f_0 , means that there isn't any change in the molecular properties. And the velocity distribution function f_0 is sampled from Maxwellian distribution.

$$f_0 = \left(\frac{m}{2\pi kT}\right)^{3/2} \exp\left[-\frac{m}{2kT}(\dot{c}_x^2 + \dot{c}_y^2 + \dot{c}_z^2)\right] \quad (20)$$

where \dot{c} refers to the thermal velocity of molecules and subscript x, y, z denotes the components. T denotes the temperature and m denotes the mass of molecules. And k refers to the Boltzmann constant.

If the expansion is made through including only the first term φ_1 , Navier Stokes equation can be obtained, and if the second term φ_2 is added, Burnett equations can be obtained [1].

2.2. DSMC Procedures

Direct Simulation Monte Carlo is based on physical simulation of representative molecules in a control volume. Each representative molecule refers to a number of real molecules so that the requirement of dilute gas assumption is born. Therefore, the method is appropriate while simulating the rarefied gas flows. In dilute gases mean free path, λ of molecules is much larger than the diameter, d of the molecules. So that treating the movement and collision of representative molecules separated in a time step, Δt is possible.

As stated before, the method needs two sets of grids in computational domain for sampling and collision processes. While forming these grids, the dimensions of

cell sizes are provided in a relation with the mean free path, λ . The reason for this is to make a guarantee of the selection of collision partners in the same cells. Supportively, choosing the molecules which are close to each other is logical in physical reality [21].

First stage of DSMC method is movement stage, and all of the representative molecules are proceeded along the time step and are transposed according to their velocities. Since the collision and movement processes are separated from each other, the time step must be chosen as being lower than the mean collision time ($\Delta t < t_c$). Thus, collision process is made become proportional to the mean collision time. And if the representative molecules trespass the wall boundaries in a time step, they are reflected in accordance with the appropriate wall reflecting model. If they exit from the inlet/outlet boundaries, they are deleted. Similarly, in this stage molecule addition process is also made through the inlet boundaries.

At the second stage, representative molecules are serialized based on grid cells. So that, the representative molecules are able to be addressed and the molecules that are locating in the same cell can be specified. This information is required for the next collision stage.

The third stage of DSMC is the collision stage with probability characteristics. In this stage, the representative molecules which are locating in the same cells, are collided with each other according to the appropriate collision model. The total mass, momentum and energy are conserved in collisions. However, the momentum and energy transfer between collided molecules are possible. On the other hand, the positions of the collided molecules are assumed invariant. DSMC method treat the collisions as binary collisions in rarefied gases. If the simulation includes chemical reactions, the reactions are treated in this stage by means of collisions.

At the final stage, macroscopic properties (pressure, temperature, density, velocity, ...etc) are evaluated via taking average of molecular properties based on

cells. If the flow is steady state flow, the time average of these properties are taken, or if the flow is transient, ensemble averaging is made on these properties. Thus, the random walks are reduced to acceptable levels.

CHAPTER 3

GEOMETRY PARAMETERIZATION

Geometry parameterization plays an important role in engineering, especially in the parametric studies like engineering design and shape optimizations. It also provides description of any geometry in mathematical sense. So, the imagination and visualization are made simplify. Similar to the definition of a basic square which can be defined by only one variable, the geometries without having a predefined geometrical shape can be described in terms of numbers. Thus, the conceptual design of any objective becomes possible. When the parameterization has been achieved, the manipulation of the geometry gets easier by only changing the suitable parameters.

In the field of aerodynamics, most of the geometries are composed of complex curvatures and so that they can not be defined via basic geometrical definitions. In this content, their definitions need higher order curvature polynomials. In such situations, the usage of space curves or conic curves may be beneficial.

On the other hand, in supersonic and hypersonic flow considerations, the shape complexity is lower than it is in subsonic flow. So, the supersonic and hypersonic vehicle geometries can be specified easily regarding to the subsonic vehicles. Generally, and especially, any conceptual hypersonic vehicle can be parameterized in terms of basic geometrical configurations such as: circular nose, angular front face, circular shoulder.

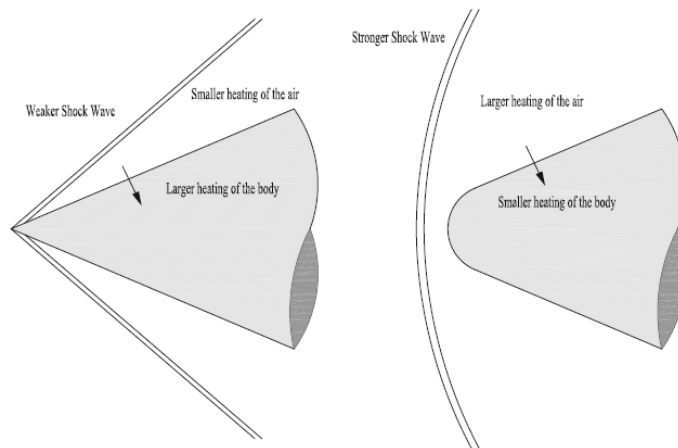


Figure 10 Comparison of flow behaviour of sharp and blunt vehicles in supersonic and hypersonic flow [22]

And these simplicities in the configuration is a conclusion of the physics of the flow field (Fig. 10). As an example, any re-entry capsule can be defined by using simple geometrical definitions (Fig. 11). And the parameters can be given as follows [22]:

- Nose radius, R_N
- Side radius, R_S
- Rear cone half angle, θ_C
- Mid radius, R_M
- Rear conical part length, L_C

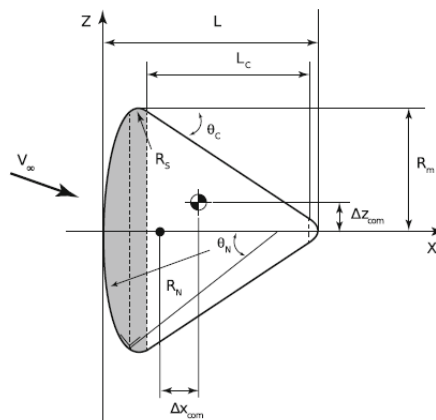


Figure 11 Schematic representation of re-entry capsule [22]

Although these definitions are sufficient for designing a re-entry capsule, the design space may be extended using cubic splines such as Bezier and B-spline curves in optimization processes. These curves are so useful while defining curvatures in two and three-dimensional spaces.

In this thesis study, B-spline curves were implemented innovatively in two-dimensional space for the optimization of Stardust re-entry capsule. Since the B-spline curves are based on Bezier basis, it would be beneficial to give some information about Bezier curves firstly.

3.1. Bezier Curves

A Bezier curve is described by its defining polygon. The defining polygon is composed of the control points of the curve, and mathematical representation can be given as follows [23]:

$$P(t) = \sum_{i=0}^n B_i J_{n,i}(t) \quad 0 \leq t \leq 1 \quad (21)$$

where the blending function or Bezier basis function is:

$$J_{n,i}(t) = \binom{n}{i} t^i (1-t)^{n-i} \quad (22)$$

In the Eqn. 21, B_i term refers to the coordinates of control points which form the control polygon of the curve. $P(t)$ term corresponds to the curve interval nodes, this means that any Bezier curve contains number of little line segments or intervals along the curve length. The number of these intervals can be adjusted via t steps, according to the expected resolution without changing the degree or the order of the curve. $J_{n,i}(t)$ refers to blending function or Bernstein basis and it is dependent on value n . The term n represents the degree of the curve, and it has to be one less than the number of control points ($n+1$).

In other words, any Bezier curve's order is equal to the number of control points, and the degree and order of the curve cannot be changed without changing the number of control points. Therefore, if the geometry to be parameterized is complex and requires many points for fitting, the resultant Bezier curve's order cannot be lowered. And this may lead to big responses in geometry across the little position changes of control points in some situations. Such situations are not wanted in optimization studies in case of difficulties in controlling the shape. To deal with this phenomenon, more advanced B-spline curves may be utilized.

3.2. B-spline Curves

Mathematically, the curve which is generated by the control points, is dependent on basis functions [23]. As stated above, Bezier curve is generated with Bezier basis. And due to the nature of Bezier basis, the order and degree of the curve is restricted with the number of control points. On the other hand, B-spline basis provide degree or order independency, so that the number of control points can be chosen arbitrarily. It also includes the Bezier basis as a special case.

Similar to Bezier curve representation, any B-spline curve is represented as follows:

$$P(t) = \sum_{i=1}^{n+1} B_i N_{i,k}(t) \quad t_{min} \leq t < t_{max}, \quad 2 \leq k \leq n + 1 \quad (23)$$

where the B-spline basis function is defined as:

$$N_{i,1}(t) = \begin{cases} 1 & \text{if } x_i \leq t < x_{i+1} \\ 0 & \text{otherwise} \end{cases} \quad (24a)$$

$$N_{i,k}(t) = \frac{(t - x_i)N_{i,k-1}(t)}{x_{i+k-1} - x_i} + \frac{(x_{i+k} - t)N_{i+1,k-1}(t)}{x_{i+k} - x_{i+1}} \quad (24b)$$

In Eqns. 23 and 24b, k refers to the order of the curve, then the degree of the curve is $k-1$, and this k value can be defined arbitrarily. In other words, order of the curve is independent from the number of control points ($n+1$). Thus, any control point along the curve has effect on significant segments, and these segments are specified through the order of the curve. As an example, any control point can only affect maximum k number of curve segments. This property presents more control on the curve.

3.2.1. B-spline Curve Fitting and Fitting Stardust Capsule

Any Bezier or B-spline curve can be generated with the equations above, since the control points B_i 's are provided. However, in most of the engineering optimization problems, the base geometry is present, and the parameterization curve must be fitted initially. When the curve is fitted, the control points coordinates are known so the deformation or modification can be made.

Considering D_i 's are, known data points of the curve to be fitted, satisfying Eqn. 23, the below expression can be written [23]:

$$[D] = [N][B] \quad (25)$$

where

$$[D]^T = [D_1(t_1) \ D_2(t_2) \ \cdots \ D_j(t_j)] \quad (26a)$$

$$[B]^T = [B_1 \ B_2 \ \cdots \ B_{n+1}] \quad (26b)$$

$$\begin{bmatrix} N_{1,k}(t_1) & \cdots & N_{n+1,k}(t_1) \\ \vdots & \ddots & \vdots \\ N_{1,k}(t_j) & \cdots & N_{n+1,k}(t_j) \end{bmatrix} \quad (26c)$$

When the above vectors and matrix (Eqn. 26a, 26b and Eqn. 26c) are obtained $[B]$ matrix, which holds the control points' coordinates can be evaluated in two steps:

$$[N]^T[D] = [N]^T[N][B] \quad (27)$$

$$[B] = [[N]^T[N]]^{-1}[N]^T[D] \quad (28)$$

And if the matrix $[N]$ is square matrix, then the Eqn. 27 would be unnecessary, and the control points could be evaluated just by multiplying Eqn. 25 with $[N]^{-1}$.

In this study, a FORTRAN code was written for fitting the Stardust geometry. LAPACK libraries were utilized for the matrix calculations. The geometry was constituted according to the dimensions in Fig. 12. Then the data points were taken from the constituted body, and the fitting procedure was followed.

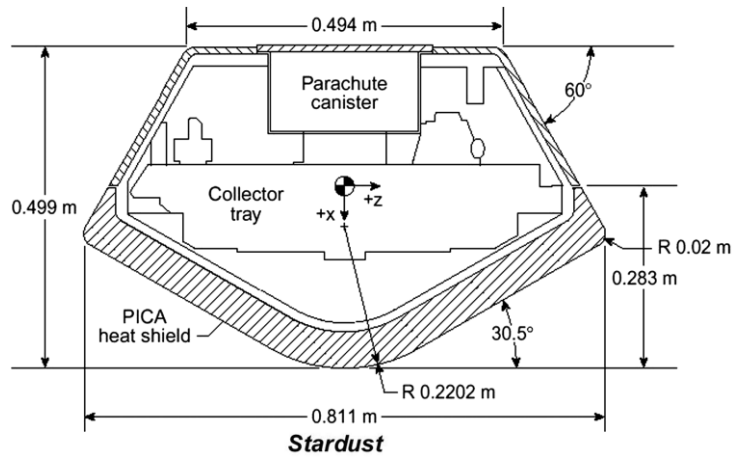


Figure 12 Stardust geometrical dimensions [24]

Curve fitting was repeated by varying the number of control points B_i 's, and the minimum number of points with good parameterization quality was searched. The minimum number of control points with good approximation quality was achieved with 37 control points, and the decrement was seen in the quality while the number was being lowered further.

To make a comparison, fitting with 15 control points which is the desired design variable number for optimization was compared with the one with 37 control points and they were plotted in Fig. 13 a and b respectively.

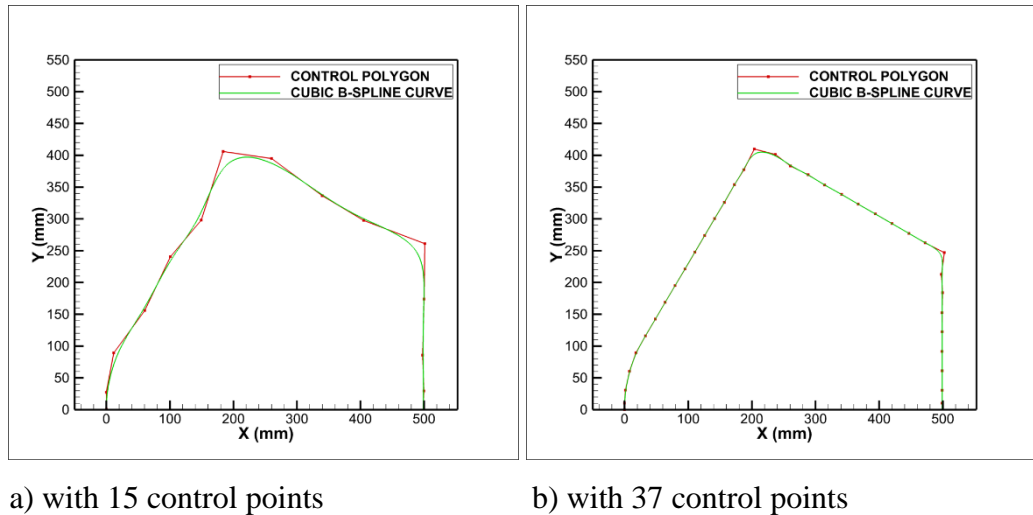


Figure 13 B-spline curve fitting of Stardust geometry

As shown from Fig. 13 a, desired fitting quality has not been able to be achieved with 15 control points. Otherwise 37 control points (Fig. 13 b) were too many to be used as design variables in the optimization study, so both satisfying the quality and also reducing the number of design variables, B-spline curves were utilized in parameterization of the geometry change rather than parameterizing the geometry itself. The following section explains the implementation procedure.

3.2.2. B-spline Parameterization of Geometry Change

First of all, the technique needs a base geometry, which is Stardust for this study, and an individual B-spline curve. Considering both as two individual curves, their intervals' coordinate points are written in vectorial form and then summed up to form another geometry vector.

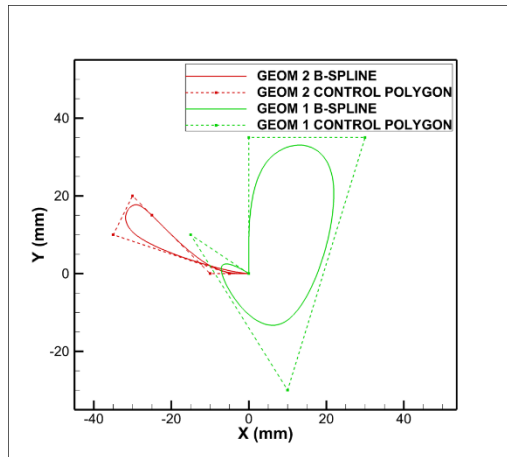


Figure 14 Control polygons and individual B-spline curves for two different geometries

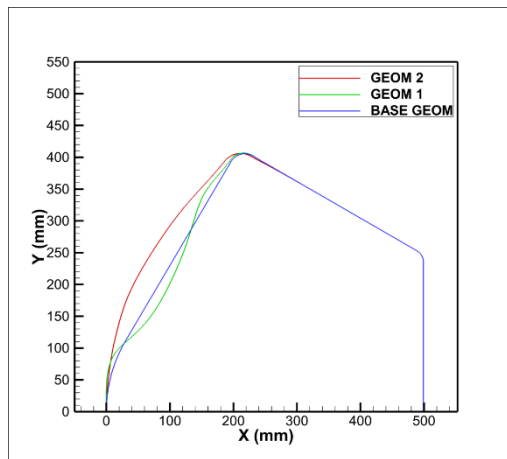


Figure 15 Base and resulting geometries

The major point is to hold the number of intervals identical (or dimension of vectors) on both curves. In this manner, if we want to obtain the same of the base geometry, the control points' coordinates and as a result, cubic spline's coordinates are filled with zeros. In Fig. 14, for geometry 1 there are only four control points different than zero, and for geometry 2 there are only five control points different than zero. This means that the geometry 1 and geometry 2 in Fig. 15 can be obtained by using only 4 and 5 control points respectively, and the rest of the points will be zero.

This procedure provides the parameterization with small number of control points. Furthermore, some of the control points affect only the aftbody of the capsule then, in the optimization of front body they are not supposed to be changed so they can be omitted. Finally, the optimization can be made by using 5 to 7 control points as the design variables.

CHAPTER 4

REDUCED ORDER MODELING

Reduced order models aim to find the dominant modes of the higher order dynamical system and use these modes for lowering the order [13]. In other words, it converts the high-fidelity high ordered physics solvers into lower ordered transfer functions. Consequently, it cuts down the computational effort significantly.

On the other hand, ROM techniques require design of experiments or solution pools which are composed of precomputed high-fidelity solutions or experiment results [17]. These solution pools can be composed of properly sampled individual solutions or be composed of arbitrarily. However, ROM accuracy is mainly dependent on the scope and uniformity of the design of experiment and the sampling methods draw a boundary to the design space and provide the individual solutions distribute in this space uniformly. Therefore, they have positive effects on the ROM accuracy.

Despite the benefits of sampling methods on the ROM accuracy, the utilization of them requires additional effort. And sometimes it requires another optimization process like adaptive sampling strategy while filling the design space.

In the present thesis study, design of experiment has been formed semi-arbitrarily. First of all, various geometries up to 40 were generated arbitrarily. While generating these geometries, design variable side constraints were used as the boundaries of the design space. In this manner, the scope of the design space has

been defined. Using this solution pool, POD-RBF based ROM model was constructed [15], [16].

A FORTRAN code was developed and LAPACK libraries were implemented in the code for matrix calculations. Using ROM model as the solver of optimization and assigning various constraint and objective functions, different geometries were obtained. These obtained geometries were simulated via DS2V and the results were compared with the ROM model's results. Then these DS2V results were added to the solution pool and this step by step process was maintained till the satisfying agreement was achieved on the results. At the end, solution pool has been composed of 90 sample solutions.

4.1. Proper Orthogonal Decomposition

POD method is such a model order reduction technique that has been widely used in the field of aerodynamics [7]–[12], [14] since its usage was introduced by Sirovich [25], [26]. It is entitled in different names such as: Karhunen Loeve Transform [27] and Principal Component Analysis [28].

Being a mathematical method, it provides orthogonal basis to a given set of data and use the effective orthogonal vectors of this basis for constructing reduced order models in terms of reconstruction, interpolation or extrapolation [5]. Because of being a mathematical method, there is no requirement to know about the source of the data and it can be applied to any suitable data set [25].

POD's linear infrastructure provides an advantage that it only requires the matrix calculations. Besides that, despite its linearity it can preserve the nonlinearity of the system.

Since POD is a mathematical tool and composed of matrix calculations, POD basis can be obtained in two different ways, either finding the eigenvalues and eigenvectors or taking singular value decomposition of data matrix. In the

following two sections, these two ways are explained. In this thesis study, POD basis was calculated through POD Snapshots approach.

4.1.1. POD Snapshots

POD Snapshot method was first introduced by Sirovich [26] and it has been known as also method of snapshots or Sirovich's method of snapshots. In Sirovich's method, each snapshot corresponds to an instantaneous flow field contour plot of turbulence structure. And the data matrix was composed of these snapshots which were written in vectorial form.

However, since the method's applicability is not restricted to transient processes whose parameter is time step, it has been able to be applied to steady state solutions with parameters different than time step. Furthermore, the snapshots can be treated as surface variables rather than flow field variables.

In this manner, considering the two-dimensional flow of Stardust re-entry, surface distributions of any of the flow variable (pressure, shear stress or heat flux) can be referred as snapshots. The important thing is to hold the number of intervals of the surface or in other words, dimensions of the snapshot vectors equal.

Considering M as the number of snapshots, and N as the number of intervals holding the flow variable, each snapshot can be written in vectorial form of dimension N . By writing each vector as column vectors of data matrix U , POD data matrix can be formed (Fig. 16). Noting that, in Fig. 16 each column corresponds to flow variable distribution of different geometry. In other words, Stardust geometry is one of the total 90 different geometries.

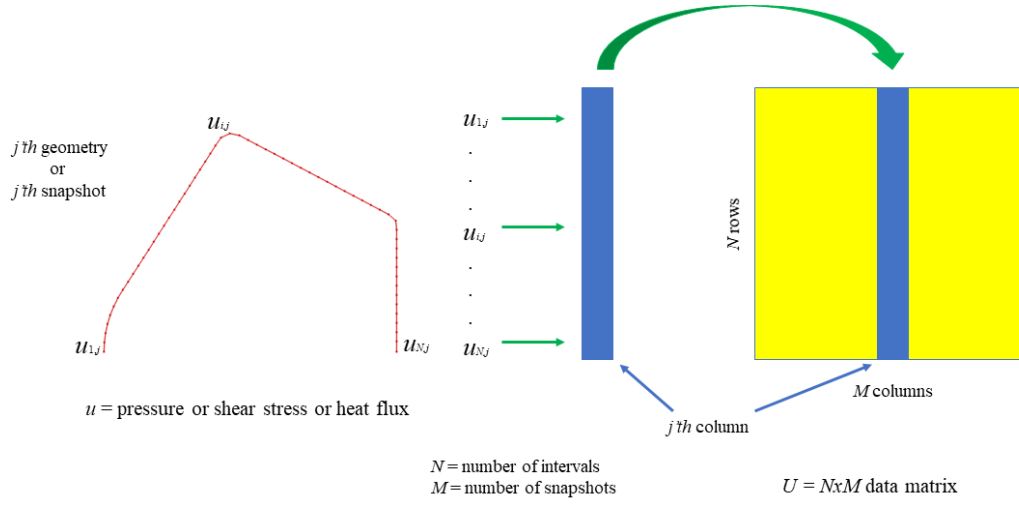


Figure 16 Forming POD data matrix

After forming the data matrix U , the procedure is followed by calculating the POD basis. Introducing correlation matrix C as below [15], [16],

$$C = U^T U \quad (29)$$

Non-trivial solution of eigenvalue problem will be the first step,

$$C V = \Lambda V \quad (30)$$

where Λ is the diagonal matrix holding the eigenvalues λ_i on its diagonal and V is the eigenvector matrix holding the eigenvectors as its column vectors. From now on the orthogonal POD basis Φ can be easily computed via the Eqn. 31.

$$\Phi = U V \Lambda^{-1/2} \quad (31)$$

This POD basis can be truncated to K number of columns where $K < M$ and the resulting matrix is shown as:

$$\hat{\Phi} = U \hat{V} \Lambda^{-1/2} \quad (32)$$

In the above expression, $\hat{\Phi}$ and \hat{V} include the first K columns of the relevant matrices. And the number K can be evaluated as holding below expression close to unity.

$$\frac{\sum_{i=1}^K \lambda_i}{\sum_{i=1}^M \lambda_i} \quad (33)$$

The obtained POD basis either original or the truncated one both must be orthogonal and provide the orthogonality condition $\Phi^T \Phi = I$, and $\hat{\Phi}^T \hat{\Phi} = I$. Once the truncated POD basis $\hat{\Phi}$ is computed, the snapshot matrix can be reconstructed or approximated according to the usage of Φ or $\hat{\Phi}$ respectively.

$$\tilde{U} = \hat{\Phi} A \quad (34)$$

In the above expression A refers to the amplitude matrix, and it can be calculated for reconstruction of U or approximation of U as \tilde{U} through the expression below:

$$A = \hat{\Phi}^T U \quad (35)$$

If K is chosen equal to M , then the $\hat{\Phi}$ is automatically changed with Φ in both Eqns. 15 and 16 and \tilde{U} is also changed with U automatically. Since $\hat{\Phi}$ is the truncated version of Φ matrix in terms of cancelling the column vectors beyond the K^{th} column.

4.1.2. POD SVD

As stated before, POD basis can be evaluated through SVD also [11]–[13], [17]. Similar to POD Snapshots, U is the data matrix. However, covariance matrix is expressed as UU^T instead of $U^T U$ this time.

$$C = UU^T \quad (36)$$

And the POD basis modes, Φ will be the eigenvector matrix of covariance matrix, C [17].

$$C = UU^T = \Phi\Lambda\Phi^{-1} \quad (37)$$

Fortunately, POD modes can be determined by taking SVD of data matrix U rather than evaluating the eigenvalues and eigenvectors of covariance matrix C .

$$U = QSX^T \quad (38)$$

where Q and X are the left and right eigenvector matrices respectively and S is the diagonal matrix containing the eigenvalues. Substituting Eqn. 38 into Eqn. 37 gives,

$$UU^T = (QSX^T)(XSQ^T) = QS^2Q^T \quad (39)$$

Then comparing the Eqns. 37 and 39, the POD basis modes will be $\Phi = Q$, and the amplitude or coefficient matrix will be $A = SX^T$, and finally the reconstruction of U data matrix can be made by the expression below:

$$U = Q(SX^T) = \Phi A \quad (40)$$

4.2. Radial Basis Functions

Radial basis functions are useful when scattered observations are present and the function to be approximated depends on many variables [29].

To eliminate the misunderstandings, the procedure that is being explained right now, is the general implementation procedure of RBFs, its application on this study, will be explained in the following section. In other words, there is not any

dependency with POD in this section neither in terms of notation nor the functions.

In a mathematical sense, RBF approximation can be defined as follows:

$$s(x) = \sum_{i=1}^n (w_i \theta(\|x - x_i\|)) \quad (41)$$

In the Eqn. 41, n refers to the number of observations, $s(x)$ is the function with parameter x to be approximated, w_i 's are the weights or coefficients of approximation, θ is the radial basis function, x is the parameter of the function to be approximated $s(x)$ and x_i 's are the parameters of observations. And the norm in the radial basis function θ is the Euclidian norm.

In order to determine the coefficients, we use the observations:

$$s(x_j) = \sum_{i=1}^n (w_i \theta(\|x_j - x_i\|)) \quad (42)$$

Since $s(x_j)$'s corresponds to the observations with parameter x_j , they are known functions. Thus, it is possible to calculate each coefficient w_i through the Eqn. 42. Despite the wide range of RBF's, the most common choices are the multiquadric and the Gaussian RBFs.

$$\theta(r) = \sqrt{r^2 + c^2} \quad (\text{multiquadric}) \quad (43a)$$

$$\theta(r) = e^{-cr^2} \quad (\text{Gaussian}) \quad (43b)$$

In the above Eqns. 43a and 43b, r refers the Euclidian norm between the parameters and c refers to smoothing factor.

4.3. POD-RBF ROM Model Development

POD methodology has been explained in POD Snapshots section. Continuing from the Eqn. 35, POD-RBF reduced order model can be explained. Referring amplitude matrix, A as the nonlinear function of the parameter vector, below expression may be written [15], [16].

$$A = BF \quad (44)$$

where F denotes the interpolation matrix, and B denotes the coefficient matrix to be determined. If we compare the Eqn. 41 and Eqn. 44, A amplitude matrix is substituted with $s(x)$, B coefficient matrix is substituted with w_i and F interpolation matrix is substituted with θ . Then interpolation matrix F can be written as,

$$F = \begin{bmatrix} f(\|\vec{p}_1 - \vec{p}_1\|) & \cdots & f(\|\vec{p}_j - \vec{p}_1\|) & \cdots & f(\|\vec{p}_M - \vec{p}_1\|) \\ \vdots & & \vdots & & \vdots \\ f(\|\vec{p}_1 - \vec{p}_i\|) & \cdots & f(\|\vec{p}_j - \vec{p}_i\|) & \cdots & f(\|\vec{p}_M - \vec{p}_i\|) \\ \vdots & & \vdots & & \vdots \\ f(\|\vec{p}_1 - \vec{p}_M\|) & \cdots & f(\|\vec{p}_j - \vec{p}_M\|) & \cdots & f(\|\vec{p}_M - \vec{p}_M\|) \end{bmatrix} \quad (45)$$

In Eqn. 45 \vec{p}_i and \vec{p}_j refer to the parameter vectors belong to i^{th} and j^{th} snapshots in the snapshot pool. These parameter vectors hold the control point coordinates of 90 different designs. The $\|\vec{p}_j - \vec{p}_i\|$ corresponds the Euclidian distance between parameter vectors, and $f()$ denotes the interpolation function or the radial basis function. By multiplying both sides of Eqn. 44 with F^{-1} , the coefficient matrix B can easily be calculated.

$$B = AF^{-1} \quad (46)$$

Noting that, the amplitude A and the coefficients B matrices are known at the moment. From now on, equating Eqn. 35 and Eqn. 44 yields,

$$\widehat{\Phi}^T U = BF \quad (47)$$

Then using the orthogonality of $\widehat{\Phi}$, the data matrix U , can be approximated as follows.

$$\widetilde{U} = \widehat{\Phi} B F \quad (48)$$

The Eqn. 48 gives the approximation of the original data matrix (snapshot matrix). However, we need a vector refers to the response solution of prospective design parameters, thus the solution would be in the shape of below,

$$\vec{u}(\vec{p}_{exp}) = \widehat{\Phi} B \vec{f}(\vec{p}_{exp}) \quad (49)$$

\vec{p}_{exp} corresponds to the prospective geometry parameter vector and it holds the control points coordinates. $\vec{f}(\vec{p}_{exp})$ is the interpolation function vector and can be evaluated via Eqn. 50.

$$\vec{f}(\vec{p}_{exp}) = \left\{ \begin{array}{c} f(\|\vec{p}_{exp} - \vec{p}_1\|) \\ \vdots \\ f(\|\vec{p}_{exp} - \vec{p}_i\|) \\ \vdots \\ f(\|\vec{p}_{exp} - \vec{p}_M\|) \end{array} \right\} \quad (50)$$

By this way, ROM model has become to be capable of providing flow variable (pressure or shear stress or heat flux) distribution solutions, $\vec{u}(\vec{p}_{exp})$ to the prospective various geometries \vec{p}_{exp} .

At the end, RBF functions have been utilized for determining the amplitudes or coefficients of POD modes. In other words, by taking advantage of RBF's ability on reflecting nonlinear system behavior, POD method has been able to be applied on hypersonic flow solutions where highly nonlinearities occur.

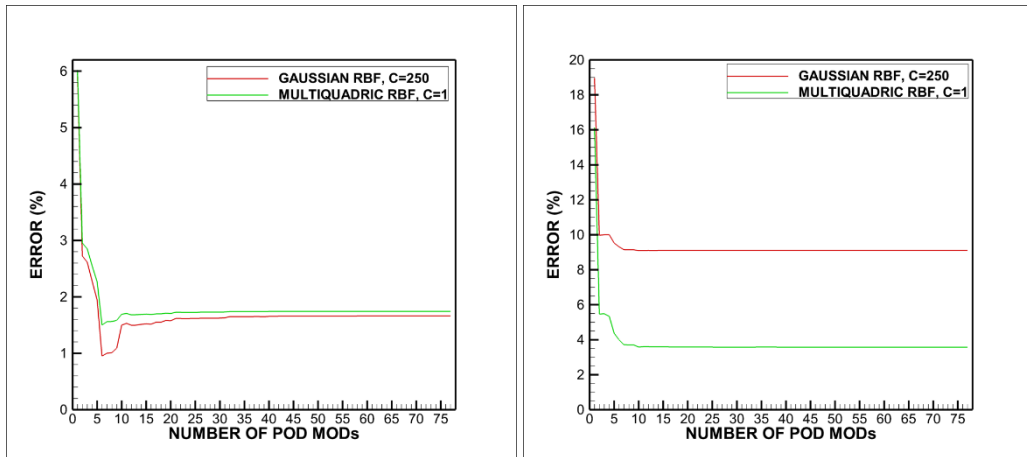
4.3.1. Comparison of RBFs

Before starting the optimization process, the selection of RBFs was made. Both multiquadric (Eqn. 43a) and Gaussian (Eqn. 43b) RBFs were implemented in the ROM model and their effects on the extrapolation capability were tested on two arbitrarily selected geometries (sample 45 and sample 75). Leave one out approach (LOO) [17] was chosen for validation, since it does not need any extra solutions. In LOO the chosen solutions are taken from the snapshot pool, and they are tried to be extrapolated via the rest of the solutions.

In Fig. 17, flow variable (pressure, shear stress and heat flux) distributions along the surface of the samples (sample 45 and sample 75) have been obtained via POD-RBF model for different number of POD mods, and they were compared with the solutions of DS2V. Both distributions from DS2V and POD-RBF ROM were written in vectorial form, and their comparisons have been made through the percentage error.

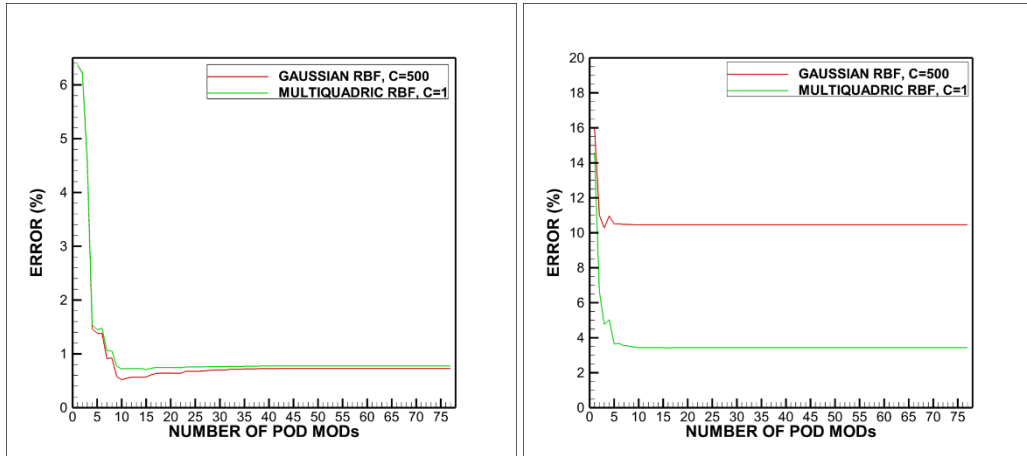
$$\%error = \frac{\|\vec{x}_{app} - \vec{x}\|}{\|\vec{x}\|} 100 \quad (51)$$

Percentage errors on the ordinates of the comparison plots (Fig. 17) were calculated through Eqn. 51. In the equation, \vec{x}_{app} refers to any flow variable distribution (pressure or shear stress or heat flux) obtained from POD-RBF, and \vec{x} refers to any flow variable distribution from DS2V.



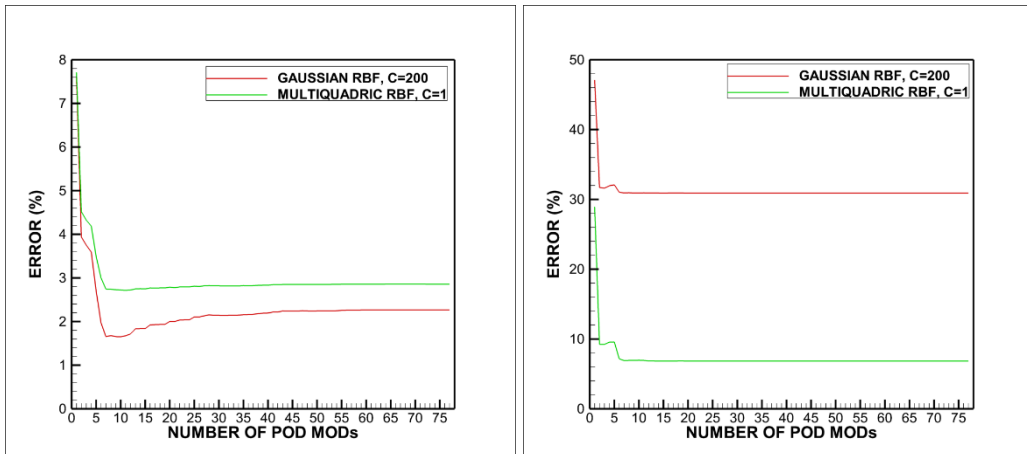
a) sample 45 heat flux distribution

d) sample 75 heat flux distribution



b) sample 45 pressure distribution

e) sample 75 pressure distribution



c) sample 45 shear stress distribution

f) sample 75 shear stress distribution

Figure 17 Error charts of multiquadric and Gaussian RBFs on sample 45 and sample 75 extrapolation

For sample 45 extrapolation the model parameter c was optimized for gaussian RBF by trial and error, and a value of 1 was used for multiquadric RBF. The optimized c values were written on the graph's legends. On the other hand, the same optimized c values of sample 45 were used in the extrapolation of sample 75.

Bearing in mind that and looking at the Fig. 17 a to e, if the parameter c is optimized for each of the extrapolation, gaussian RBF can provide more accurate predictions than the multiquadric RBF. However, if they are not optimized, the percentage error of Gaussian RBF can increase up to the range of %30's. To this respect, due to its stable error characteristics, multiquadric RBF were chosen instead of gaussian RBF.

CHAPTER 5

GRADIENT BASED OPTIMIZATION

Generally, an optimization problem can be defined in mathematical sense as follows [19]:

Minimizing or maximizing the objective function:

$$F(X) \quad \text{objective function} \quad (52)$$

Subject to constraints:

$$g_j(X) \leq 0, \quad j = 1, m \quad \text{inequality constraints} \quad (53)$$

$$X_i^L \leq X_i \leq X_i^U, \quad i = 1, n \quad \text{side constraints} \quad (54)$$

Design variables:

$$X = \begin{Bmatrix} X_1 \\ X_2 \\ X_3 \\ \vdots \\ X_n \end{Bmatrix} \quad \text{design variables} \quad (55)$$

while $F(X)$ and $g_j(X)$ refer to the objective and constraint functions, side constraints are not functions and they are required for defining the limit boundaries of each design variables X_i , in other words they are required for specifying the design space. On the other hand, objective and constraint functions

are the functions and they can be linear or nonlinear functions. Furthermore, their calculations may be made by analytically or numerically.

Noting that, constraint functions are defined as inequality condition, and if the equality is desired, it must be defined in terms of defining two inequality constraints.

The optimization procedure starts from an initial set of design variables, X^0 [30]. After starting the optimization, design variables are modified in each iteration until the optimum design point is reached.

$$X^q = X^{q-1} + \alpha^* S^q \quad (56)$$

In the Eqn. 56, q in the superscript denotes the iteration number, S denotes the search direction vector and α^* denotes the distance in the search direction.

5.1. Optimization Procedure

Stardust's front face optimization has been conducted, considering drag force, maximum heat flux value, total heating energy and volume of the re-entry. These four functions were specified initially and assigning them as objective and constraint functions varyingly, various optimization cases were obtained. Stardust geometry was defined as the initial geometry and various geometries were produced with B-spline subroutine.

As stated in the Chapter 2, B-spline subroutine had been written as producing the geometries by means of geometry change. So, the required base geometry coordinates were read as an input vector to the subroutine (Fig. 18). After reading base geometry vector, it produces geometry according to the geometry parameters (B-spline control points) that come from EVAL subroutine.

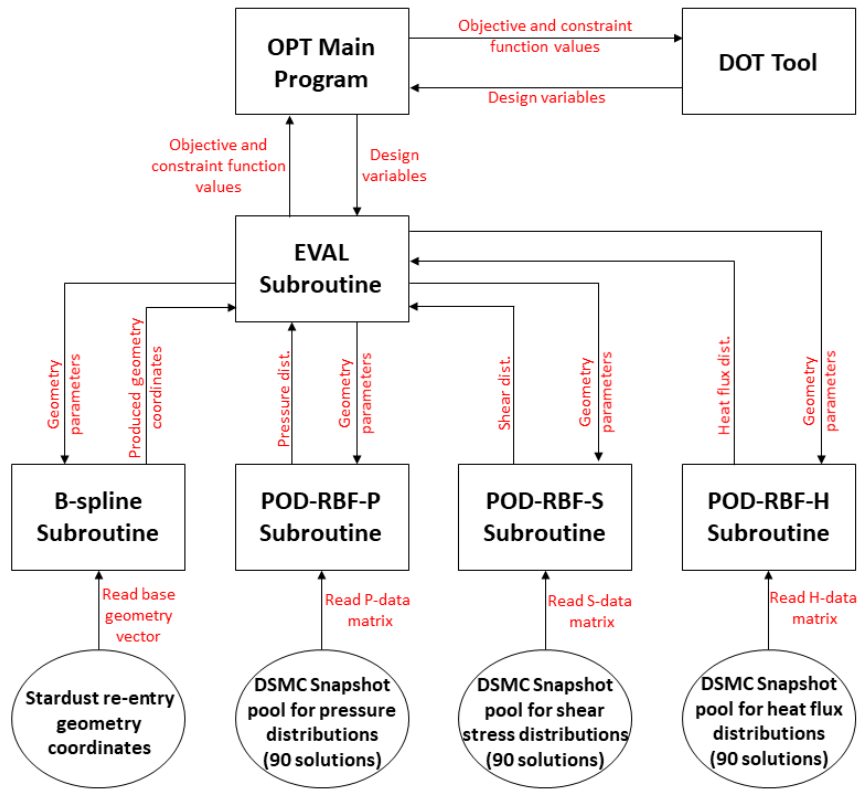


Figure 18 Optimization scheme

EVAL subroutine works as the manager of the optimization (Fig. 18). It evaluates the volume of the re-entry geometry by integrating the geometry coordinates from B-spline subroutine. Furthermore, it receives the pressure, shear stress and heat flux distributions from POD-RBF-P, POD-RBF-S and POD-RBF-H subroutines respectively and integrates these distributions over the surface of the geometry for calculating the total values of pressure, shear stress and heat energy. It evaluates the drag force by summing up the total pressure and total shear stress. Also, it evaluates the maximum value of heat flux. Thus, the all of the pre-defined functions such as: total drag, total heating energy, maximum heat flux value and volume of geometry are evaluated and are sent to OPT program for the next step.

OPT program takes these values and transfers to DOT tool and takes the information of next step. The mentioned information holds the geometry parameters of new geometry in terms of design variables. Noting that, design variables are composed of specified number of B-spline control points. However,

the geometry parameters in Fig. 18 contain the all of 15 B-spline control points. As stated in the Chapter 2 the parameterization had been made by total of 15 control points. On the other hand, as being design variables 7 control points corresponding to the front face of re-entry were chosen out of 15 control points. Due to this, design variables and geometry parameters were defined separately. In this manner, 7 of the geometry parameters were defined from the design variables, and the rest of them were assigned as zeros.

DSMC snapshot pools were composed of 90 different geometries' DS2V simulations. Since the flow field solutions are not required, they contain the surface distributions of pressure, shear stress and heat flux. Each distribution solution is defined as column vector and they compose matrix together. These matrices are read from POD-RBF subroutines.

CHAPTER 6

RESULTS AND DISCUSSION

6.1. DSMC Flow Simulation Validation

Before going into optimization, the flow field solution of Stardust body was compared with analogous CFD and DSMC studies.

6.1.1. Simulation Conditions

The freestream conditions of the trajectory point can be found from the available spectral measurements during Stardust entry and are presented in Table 1. Corresponding Knudsen number of the flow lies in a region where the continuum breakdown occurs. This lets us the comparison of the study with both CFD and DSMC calculations in the literature.

Table 1 Freestream conditions at 81 km altitude [24]

<i>Freestream temp, K</i>	217.6
<i>Freestream number density, molecules/m³</i>	2.64E+20
<i>Freestream velocity, m/s</i>	12385
<i>Freestream O₂ mole fraction %</i>	23.67
<i>Freestream N₂ mole fraction %</i>	76.23
<i>Freestream Knudsen number</i>	0.005

Eleven species real air model was used for including the effects of nonequilibrium aerothermodynamics. The chemical reaction set with 41 equations (Table 2) was used. Recombination of particles (atoms, ions and molecules) in the flow-field and ablation of surface were neglected; however, the dissociation, exchange and ionization reactions were implemented in the calculations. While forebody surface of the re-entry was assumed as fully catalytic to recombination of atoms, ions and

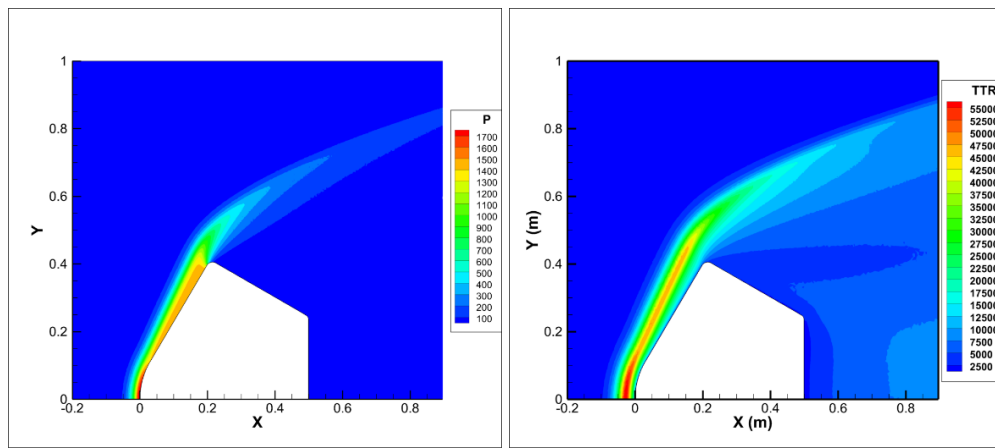
electrons, the aft body was assumed as noncatalytic. The constant wall temperature of 2000 K was attended for the forebody surface while 900 K was attended for the aft body surface.

Table 2 List of chemical reactions [31]

No	Reaction (Energy in J)	Rate Coefficient ($m^3/molecule\ s$)
1.	$O_2 + N + 8.197x10^{-19} \rightarrow 2O + N$	$1.375x10^{-10}T^{-1}\exp(-59370/T)$
2.	$O_2 + NO + 8.197x10^{-19} \rightarrow 2O + NO$	$4.58x10^{-11}T^{-1}\exp(-59370/T)$
3.	$O_2 + N_2 + 8.197x10^{-19} \rightarrow 2O + N_2$	$4.58x10^{-11}T^{-1}\exp(-59370/T)$
4.	$2O_2 + 8.197x10^{-19} \rightarrow 2O + O_2$	$4.58x10^{-11}T^{-1}\exp(-59370/T)$
5.	$O_2 + O + 8.197x10^{-19} \rightarrow 3O$	$1.375x10^{-10}T^{-1}\exp(-59370/T)$
6.	$N_2 + O + 1.561x10^{-18} \rightarrow 2N + O$	$1.85x10^{-8}T^{-1.6}\exp(-113000/T)$
7.	$N_2 + O_2 + 1.561x10^{-18} \rightarrow 2N + O_2$	$6.17x10^{-9}T^{-1.6}\exp(-113000/T)$
8.	$N_2 + NO + 1.561x10^{-18} \rightarrow 2N + NO$	$6.17x10^{-9}T^{-1.6}\exp(-113000/T)$
9.	$2N_2 + 1.561x10^{-18} \rightarrow 2N + N_2$	$6.17x10^{-9}T^{-1.6}\exp(-113000/T)$
10.	$N_2 + N + 1.561x10^{-18} \rightarrow 3N$	$1.85x10^{-8}T^{-1.6}\exp(-113000/T)$
11.	$NO + N_2 + 1.043x10^{-18} \rightarrow N + O + N_2$	$3.83x10^{-13}T^{-0.5}\exp(-75550/T)$
12.	$NO + O_2 + 1.043x10^{-18} \rightarrow N + O + O_2$	$3.83x10^{-13}T^{-0.5}\exp(-75550/T)$
13.	$NO + NO + 1.043x10^{-18} \rightarrow N + O + NO$	$3.83x10^{-13}T^{-0.5}\exp(-75550/T)$
14.	$NO + O + 1.043x10^{-18} \rightarrow N + 2O$	$7.66x10^{-13}T^{-0.5}\exp(-75550/T)$
15.	$NO + N + 1.043x10^{-18} \rightarrow 2N + O$	$7.66x10^{-13}T^{-0.5}\exp(-75550/T)$
16.	$NO + O + 2.19x10^{-19} \rightarrow N + O_2$	$3.6x10^{-22}T^{1.29}\exp(-19700/T)$
17.	$N_2 + O + 5.175x10^{-19} \rightarrow N + NO$	$5.3x10^{-17}T^{0.1}\exp(-37500/T)$
18.	$O_2 + N \rightarrow 2.19x10^{-19} + O + NO$	$5.2x10^{-22}T^{1.29}\exp(-3600/T)$
19.	$NO + N \rightarrow 5.175x10^{-19} + O + N_2$	$2.02x10^{-17}T^{0.1}$
20.	$N + O + 4.442x10^{-19} \rightarrow NO^+ + e^-$	$2.55x10^{-20}T^{0.37}\exp(-32030/T)$
21.	$O + e^- + 2.18x10^{-18} \rightarrow O^+ + 2e^-$	$3.00x10^{-12}\exp(-157900/T)$
22.	$O + O + 1.12x10^{-18} \rightarrow O_2^+ + e^-$	$6.42x10^{-22}T^{0.49}\exp(-81100/T)$
23.	$O_2^+ + e^- \rightarrow 1.12x10^{-18} + O + O$	$3.83x10^{-9}T^{-1.51}$
24.	$O + O_2^+ + 2.57x10^{-19} \rightarrow O^+ + O_2$	$1.89x10^{-16}T^{-0.52}\exp(-18760/T)$
25.	$O^+ + O_2 \rightarrow 2.57x10^{-19} + O + O_2^+$	$1.89x10^{-16}T^{-0.52}$
26.	$N^+ + N_2 + 1.67x10^{-19} \rightarrow N + N_2^+$	$1.67x10^{-17}T^{-0.18}\exp(-12100/T)$
27.	$O + NO^+ + 7.04x10^{-19} \rightarrow O^+ + NO$	$4.58x10^{-17}T^{0.01}\exp(-51000/T)$
28.	$N + N + 9.34x10^{-19} \rightarrow N_2^+ + e^-$	$2.98x10^{-20}T^{0.77}\exp(-67650/T)$
29.	$N + e^- + 2.33x10^{-18} \rightarrow N^+ + 2e^-$	$1.00x10^{-14}\exp(-168800/T)$
30.	$O^+ + NO \rightarrow 7.04x10^{-19} + O + N_2^+$	$1.97x10^{-17}T^{0.01}$
31.	$O^+ + N_2 + 3.06x10^{-19} \rightarrow O + N_2^+$	$1.06x10^{-16}T^{-0.21}\exp(-22160/T)$
32.	$N_2^+ + e^- \rightarrow 9.34x10^{-19} + N + N$	$8.88x10^{-10}T^{-1.23}$
33.	$NO^+ + e^- \rightarrow 4.42x10^{-19} + N + O$	$4.03x10^{-9}T^{-1.63}$
34.	$N_2^+ + N \rightarrow 1.66x10^{-19} + N^+ + N_2$	$2.37x10^{-18}T^{-0.52}$
35.	$N_2^+ + O \rightarrow 3.15x10^{-19} + O^+ + N_2$	$1.77x10^{-17}T^{-0.21}$
36.	$N + NO^+ + 8.43x10^{-19} \rightarrow N^+ + NO$	$1.84x10^{-15}T^{-0.02}\exp(-61060/T)$
37.	$N^+ + NO \rightarrow 8.43x10^{-19} + N + NO^+$	$1.84x10^{-15}T^{-0.02}$
38.	$O_2 + NO^+ + 4.47x10^{-19} \rightarrow NO + O_2^+$	$1.72x10^{-14}T^{-0.17}\exp(-32400/T)$
39.	$NO + N^+ \rightarrow 4.47x10^{-19} + NO^+ + N$	$4.47x10^{-15}T^{-0.17}$
40.	$N + NO^+ + 4.9x10^{-19} \rightarrow O + N_2^+$	$2.83x10^{-17}T^{0.4}\exp(-35500/T)$
41.	$O + N_2^+ \rightarrow 4.9x10^{-19} + N + NO^+$	$4.1x10^{-18}T^{0.4}$

6.1.2. Validation of Simulation

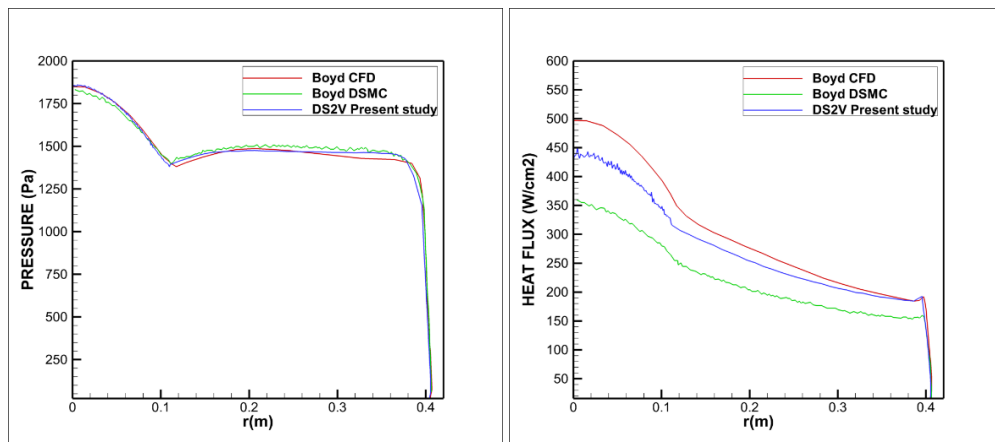
Thermodynamic temperature is the measure of energy in all flow regimes. However, in molecular regime, temperature is quantized and is split into translational, rotational, vibrational and electrical partitions. In this manner, translational temperature becomes the measure of kinetic energy associated with thermal velocities, while the rotational, vibrational and electrical temperatures become the measure of internal energies [4]. To this end, translational temperature was regarded rather than temperature on the contour graphs.



a) Pressure contours

b) Translational temperature contours

Figure 19 Contour plots of Stardust



a) Pressure distribution plot

b) Heat flux distribution plot

Figure 20 Comparison of pressure and heat flux distributions [24]

Fig. 19 shows the pressure and translational temperature contours of Stardust re-entry from DS2V, and Fig. 20 shows the comparison of pressure and heat flux distributions. Pressure and heat flux distributions were compared with the ref. [24]'s CFD and DSMC solutions. According to Fig. 20 a and b, very good agreement was achieved on pressure distributions, and heat flux distributions lie on the averaged line of the ref's DSMC and CFD solutions. Thus, the results' validity has been found as sufficient to continue the optimization process.

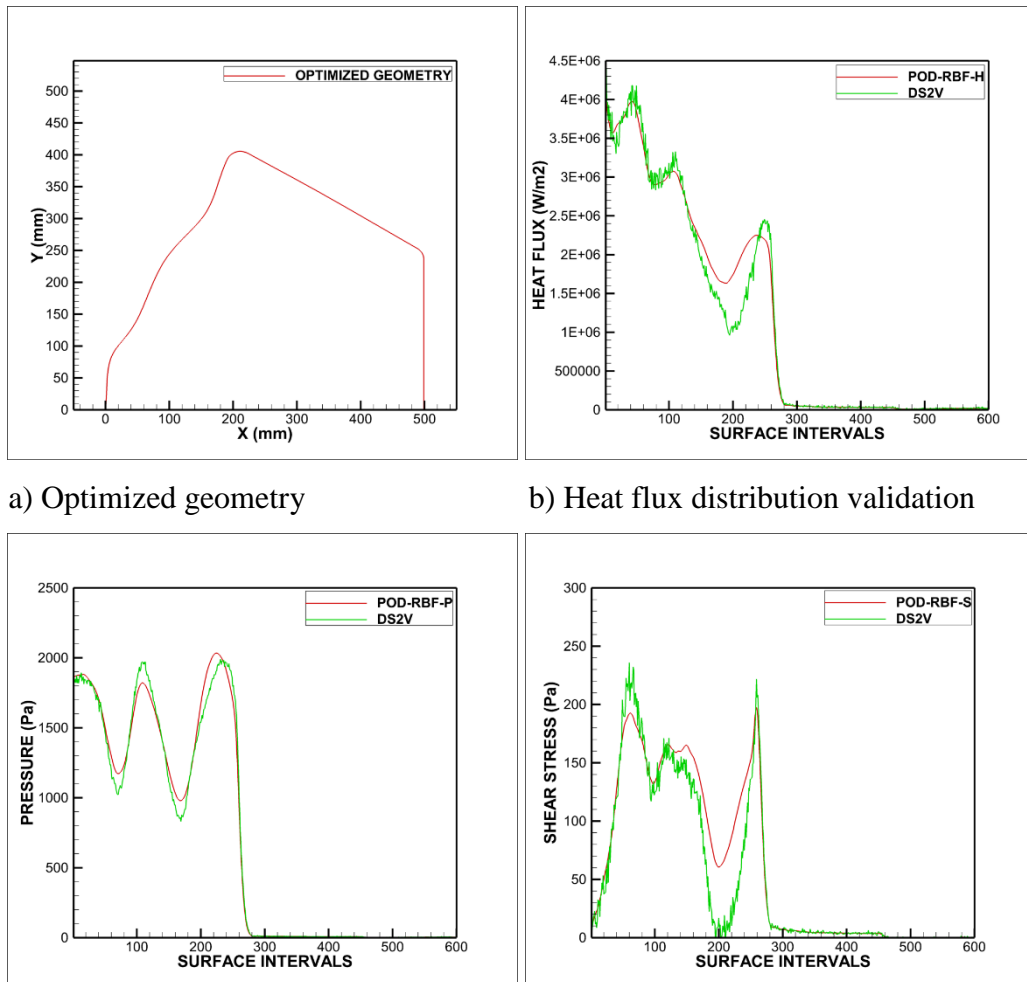
6.2. Optimization Results

Optimization studies were conducted on four cases such as: maximizing drag force, minimizing heating energy, minimizing maximum heat flux and maximizing the volume. These four objectives were used as constraints also by leaving alone the objective function. In other words, for the first case, while maximization of drag was the objective function, heat energy, maximum heat flux and the volume were implemented as constraints. Constraints' limit values were held as equal to Stardust's values and side constraints were implemented for constraining the region of design variables.

In all the cases, the front surface of the body was aimed to be optimized so the 7 control points out of total 15 control points were defined as the design variables. These 7 points are those that are responsible for the shape of the front surface. All the cases were initialized from the base Stardust geometry. Additionally, the maximum diameter of the geometry and the location were bounded in a tight space in terms of side constraints, by restricting significant changes in the shape due to the concerns of the snapshot pool scope. When the all four optimized geometries were obtained, they were simulated with DS2V for validation and the results were plotted for comparison.

6.2.1. Optimized Geometry Solutions Validation

Optimized geometries and their flow variable distributions were given in figures (Fig. 21 to Fig. 24). The plots contain the DS2V results also for seeing the extrapolation capability of POD-RBF. Additionally, comparative integrated values were expressed in tabulated form in Table 3 to Table 6. Noting that, DS2V flow variable distribution results were filtered via MATLAB's curve fitting tool before taking their integrations due to noise. This procedure was not required for ROM solutions since they are not noisy. For information, filtration process was indicated on the tables.



a) Optimized geometry

b) Heat flux distribution validation

c) Pressure distribution validation

d) Shear stress distribution validation

Figure 21 Case 1 maximizing drag optimization results validation (Opt. geom. 1)

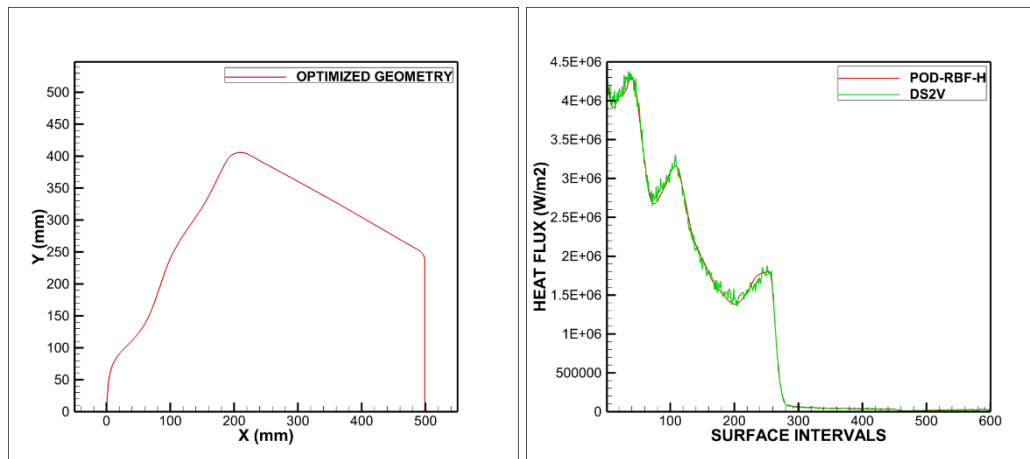
Table 3 Validation of case 1 maximizing drag on tabulated results (Opt. Geom. 1)

<i>METHOD</i>	<i>PRES. FORCE (N)</i>	<i>SHEAR FORCE (N)</i>	<i>TOT. DRAG FORCE (N)</i>	<i>MAX. HEAT FLUX (W/m²)</i>	<i>TOT. HEAT ENERGY (W)</i>	<i>VOLUME (m³)</i>
POD-RBF	782.48	44.10	826.58	4035206	1376951	0.14483
DS2Vfiltered	774.20	36.49	810.69	4050300	1273461	0.14483
% ERROR	1.07	20.86	1.96	0.37	8.13	-

For the first case, total drag force was defined as objective function to be maximized. On the other hand, volume, maximum heat flux and total heating energy values were defined as constraints, and the Stardust re-entry's values were assigned to these constraints. Fig. 21 shows the optimization results in terms of optimized geometry and comparative flow variable distributions over the surface. And Table 3 shows the integrated values in comparison.

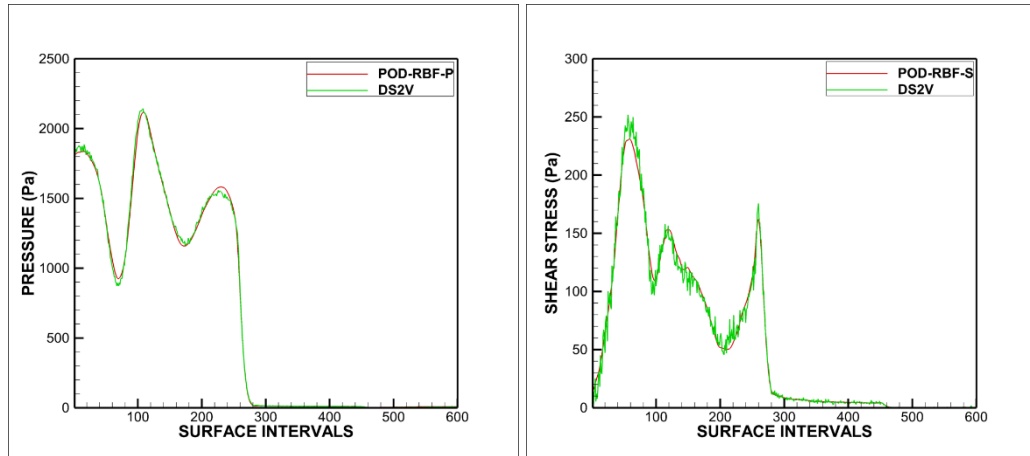
According to Fig. 21 b heat flux distribution plot, very good agreement was achieved at the region from nose to mid front face. Supporting this agreement, the error percentage in maximum heat flux value was found as 0.37 % (Table 3). However, the agreement starts deviation while approaching to shoulder. And this inconsistency results the error percentage in total heating energy reach up to 8.13 % (Table 3).

On the other hand, very good agreement was able to be achieved in the pressure distribution in Fig. 21 c and the error percentage was found as 1.07 % in pressure force (Table 3). Additionally, good agreement was achieved in shear stress distribution except the region between 150th and 250th intervals of surface (Fig. 21 d). This region corresponds to the same shoulder region where the disagreement of heat flux distribution is present (Fig. 21 b). However, this region affects the integrated value of shear stress more than the integration of heat flux. Shear stress's very low numerical values relative to heat flux, is responsible for the bigger error percentages in comparison (Table 3).



a) Optimized geometry

b) Heat flux distribution validation



c) Pressure distribution validation

d) Shear stress distribution validation

Figure 22 Case 2 minimizing heat energy optimization results validation

(Opt. Geom. 2)

Table 4 Validation of case 2 minimizing heat energy on tabulated results

(Opt. Geom. 2)

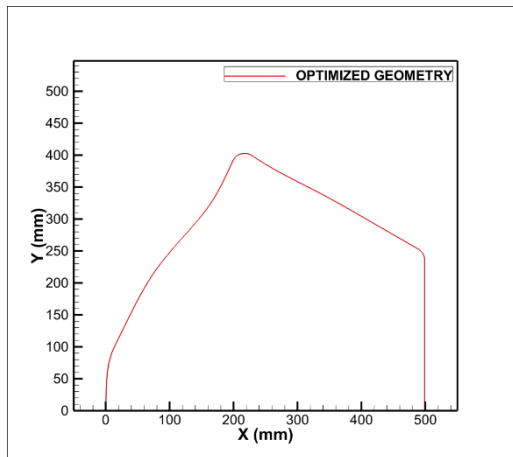
<i>METHOD</i>	<i>PRES. FORCE (N)</i>	<i>SHEAR FORCE (N)</i>	<i>TOT. DRAG FORCE (N)</i>	<i>MAX. HEAT FLUX (W/m²)</i>	<i>TOT. HEAT ENERGY (W)</i>	<i>VOLUME (m³)</i>
POD-RBF	736.96	37.75	774.71	4314062	1243186	0.14561
DS2Vfiltered	738.43	37.75	776.19	4316500	1245550	0.14561
% ERROR	0.20	0.01	0.19	0.06	0.19	-

In this second case, total heating energy was defined as objective function to be minimized. And volume, maximum heat flux and total drag values were defined

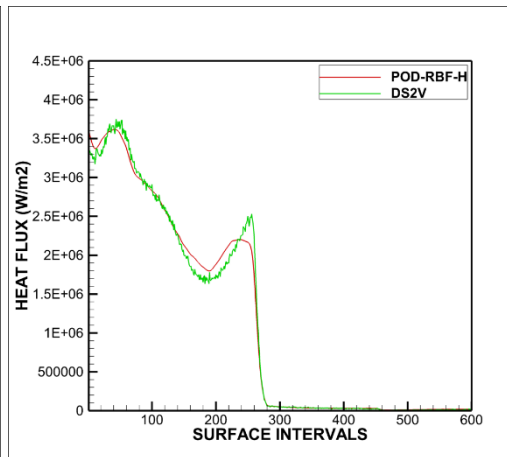
as constraints, and the Stardust re-entry's values were assigned to these constraints.

According to Fig. 22 b, c and d and Table 4, excellent agreement was achieved between DS2V and POD-RBF model. And the results consistency can be seen without the requirement of comment. Interpretations may be made on why the same consistency was not able to be achieved in the first optimization case while the both optimized geometries look similar (Fig. 21 a and Fig. 22 a). This may be explained through the conditions which ROM's accuracy is dependent.

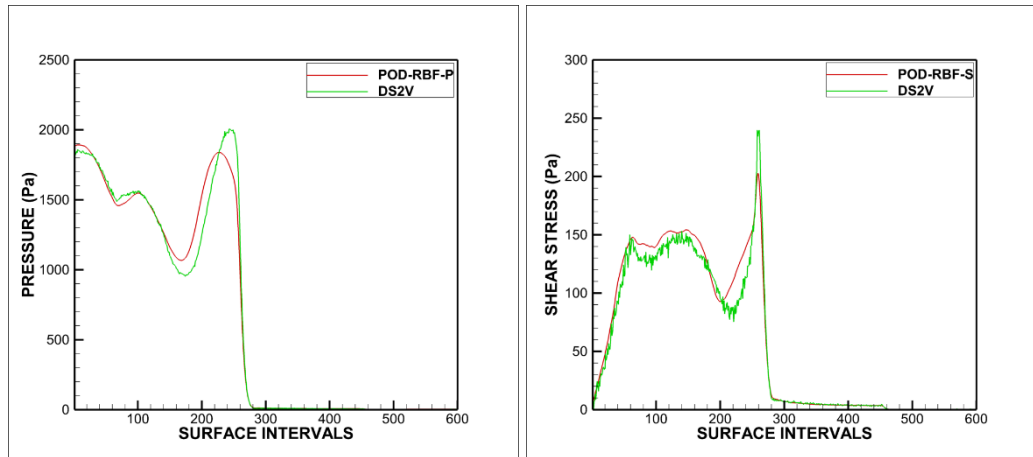
Remembering that, the approximation accuracy of ROMs had been dependent on the scope of the snapshot pool and on the uniqueness of the samples. However, any well accepted method was not implemented in this study while forming the solution pool, and the sampling was made arbitrarily. Possibly, relatively more concave region (just before the shoulder) of opt. geom. 1, takes its geometry parameters out of the scope of the snapshot pool and this reduces the approximation accuracy.



a) Optimized geometry



b) Heat flux distribution validation



c) Pressure distribution validation

d) Shear stress distribution validation

Figure 23 Case 3 minimizing maximum heat flux optimization results validation

(Opt. Geom. 3)

Table 5 Validation of case 3 minimizing maximum heat flux on tabulated results

(Opt. Geom. 3)

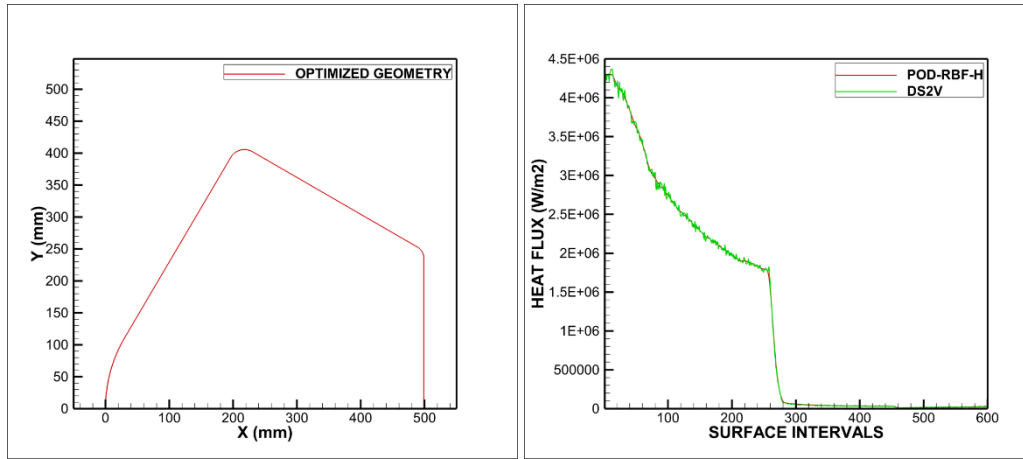
<i>METHOD</i>	<i>PRES. FORCE (N)</i>	<i>SHEAR FORCE (N)</i>	<i>TOT. DRAG FORCE (N)</i>	<i>MAX. HEAT FLUX (W/m²)</i>	<i>TOT. HEAT ENERGY (W)</i>	<i>VOLUME (m³)</i>
POD-RBF	728.28	48.78	777.07	3618034	1376139	0.14532
DS2Vfiltered	719.18	47.19	766.37	3680700	1358001	0.14532
% ERROR	1.27	3.37	1.40	1.70	1.34	-

In the third case, objective function was changed to minimization of the maximum heat flux. And volume, total heating energy and total drag values were defined as constraints, and the Stardust re-entry's values were assigned to these constraints.

By looking at Fig. 23, almost very good agreement was achieved in heat flux, pressure and shear stress distribution plots. However, there is a concave region near shoulder of opt. geom. 3, similar to opt. geom. 1. And the distribution plots deviate in this region like as they do in the first case (Fig. 21 and Fig. 23). This deviation validates the comment made about the scope of snapshot pool.

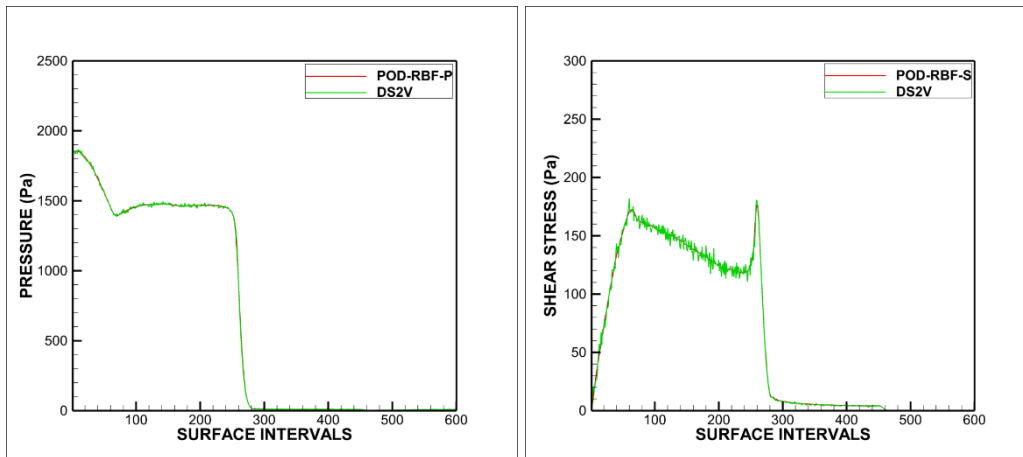
On the other hand, slighter concave region of opt. geom. 3 relative to opt. geom. 1 (Fig. 21 a and Fig. 23 a) provides itself be inside of the scope of snapshot pool.

Consequently, the error percentages were remained at the acceptable levels (Table 5).



a) Optimized geometry

b) Heat flux distribution validation



c) Pressure distribution validation

d) Shear stress distribution validation

Figure 24 Case 4 maximizing volume optimization results validation

(Opt. Geom. 4)

Table 6 Validation of case 4 maximizing volume on tabulated results

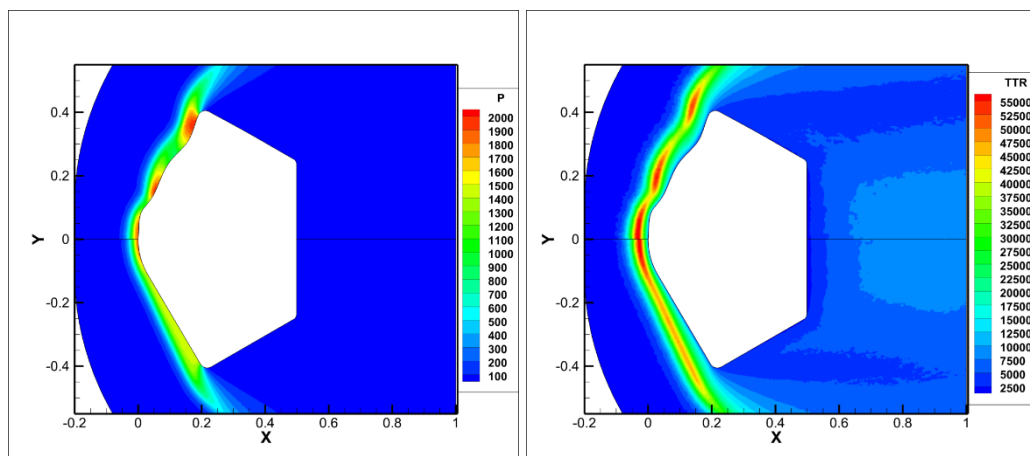
(Opt. Geom. 4)

<i>METHOD</i>	<i>PRES. FORCE (N)</i>	<i>SHEAR FORCE (N)</i>	<i>TOT. DRAG FORCE (N)</i>	<i>MAX. HEAT FLUX (W/m²)</i>	<i>TOT. HEAT ENERGY (W)</i>	<i>VOLUME (m³)</i>
POD-RBF	727.91	48.33	776.24	4302083	1374997	0.14519
DS2Vfiltered	727.94	48.29	776.22	4308100	1373604	0.14519
% ERROR	0.004	0.083	0.003	0.140	0.101	-

In the fourth case, objective function was changed to maximization of the volume while the Stardust re-entry's max heat flux, total heating energy and total drag force values were defined as the constraint functions. However, under these conditions there was not a change in the shape of the geometry (Fig. 24 a). In addition to this, having the same geometry solution in the snapshot pool provided an excellent approximation accuracy of ROM model. The agreement quality can be seen from Fig. 24 b, c and d and also from Table 6.

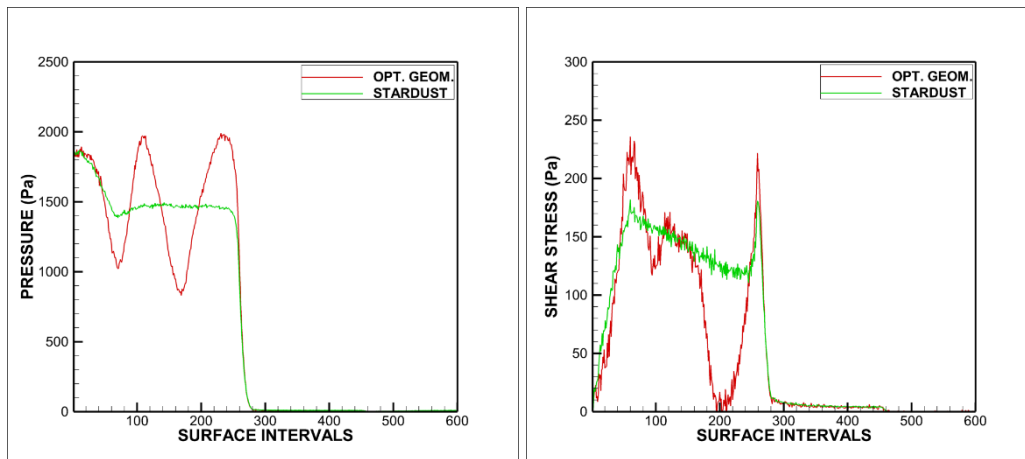
6.2.2. Comparison of Stardust and Optimized Geometries

In this section of the Chapter 6, the optimized geometries' DS2V results were compared with the Stardust re-entry's DS2V results. Pressure and translational contours of optimized geometries were plotted in mirrored form with Stardust (Fig. 25 to Fig. 27 a and b). Pressure, heat flux and shear stress distributions of both Stardust and optimized geometries were also plotted in the same graphs for comparison (Fig. 25 to Fig. 27 c, d and e). And their integrated values were also given in tables (Table 7 to Table 9). Objective and constraint functions were indicated on the tables. Fourth case was not given due to having the same geometry with the Stardust re-entry. The noisy distributions were filtered with MATLAB curve fitting tool before integration.



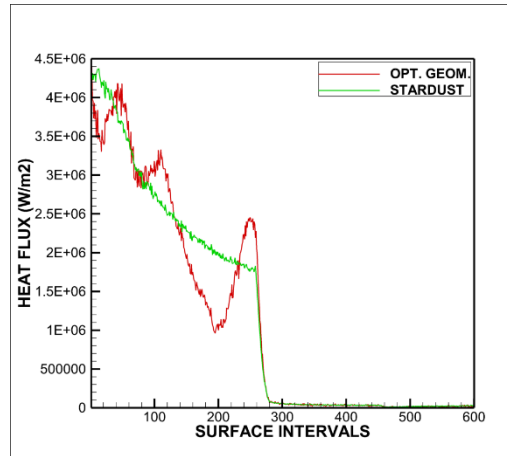
a) Pressure contours

b) Translational temperature contours



c) Pressure distribution

d) Shear stress distribution



e) Heat flux distribution

Figure 25 Comparison of Stardust and Opt. geom. 1

Table 7 Tabulated results of Stardust and Opt. geom. 1

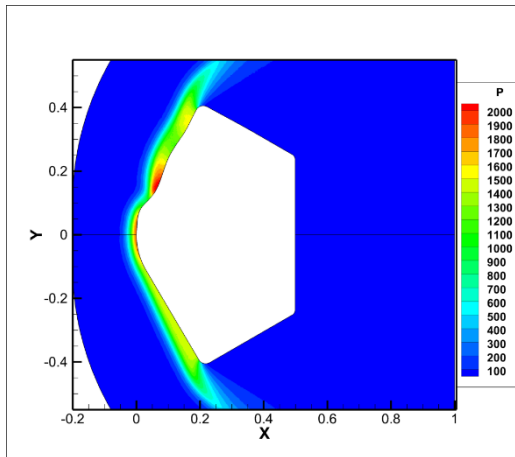
<i>GEOMETRY</i>	<i>PRES. FORCE(N)</i>	<i>SHEAR FORCE(N)</i>	<i>TOT. DRAG FORCE(N) OBJ. FUNC. (max.)</i>	<i>MAX. HEAT FLUX(W/m²) CONST.</i>	<i>TOT. HEAT ENERGY(W) CONST.</i>	<i>VOLUME (m³) CONST.</i>
STARDUST	727.94	48.29	776.22	4308100	1373604	0.14519
OPT.GEOM.1	774.20	36.49	810.69	4050300	1273461	0.14483

By aiming the maximization of drag force, Opt. geom. 1 was found. Constraints and the objective function were indicated on the Table 7. The drag force was increased, maximum heat flux and total heating energy were decreased, and the volume was preserved.

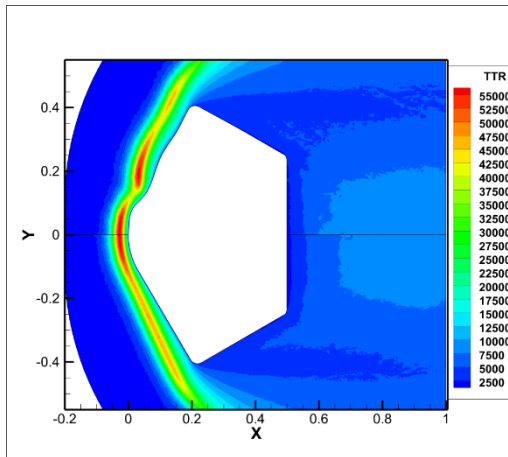
According to Fig. 25 a and b, the shock core is split into three regions, due to wavy front surface. It is realizable from Fig. 25 a, c and d that, concavities increase pressure and decrease shear stress dramatically. In Fig. 25 c, these increments can be seen from the second and third peaks. Similarly, sudden decrements in the shear stress can be seen over the same intervals in Fig. 25 d.

Due to stagnation points at the nose and at the concave regions pressure distribution makes peaks (Fig. 25 c). Inversely, shear stress makes opposite peaks at the stagnation points (Fig. 25 d). Considering the inverse relation between flow speed and pressure, and the expression of shear stress ($\tau = \mu \frac{du}{dy}$), the relation between pressure and shear stress can be understood clearly. Since the flow speed increases while passing over convexities and, decreases while passing over concavities, sudden increments and decrements occur in pressure and shear stress distribution plots (Fig. 25 c and d).

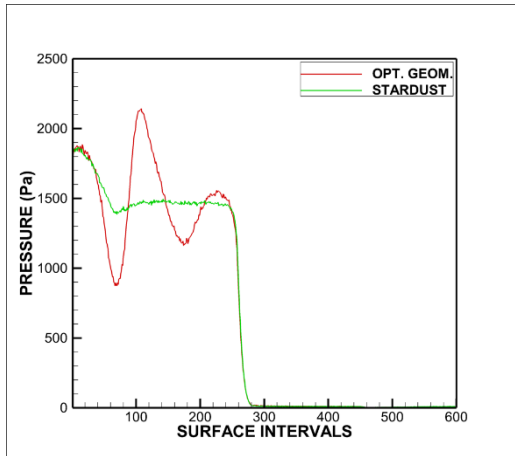
On the other hand, by the help of blunter nose, thermal shock core is slightly pushed further (Fig. 25 b) in comparison with Stardust's. This results the lower maximum heat flux value at the nose of the geometry (Fig. 25 e and Table 7). Wavy surface of the geometry causes splitting at the shock core (Fig. 25 b). And these split shock cores preserve the high temperature in their core (red regions in Fig. 25 b). These high temperature effects cause the peaks in the heat flux distribution (Fig. 25 e). However, despite these peaks, thermal shock cores are located far from geometry surface and as a result, the total heating energy is reduced (Table 7).



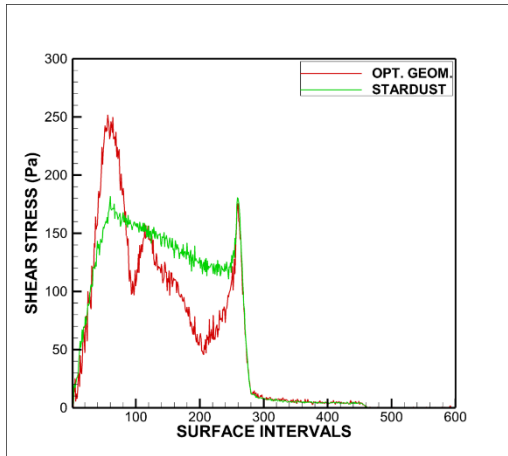
a) Pressure contours



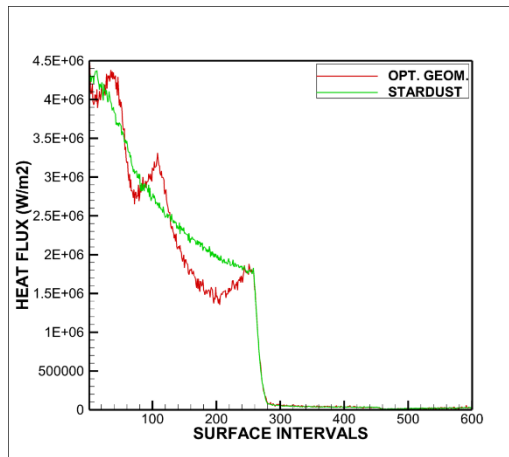
b) Translational temperature contours



c) Pressure distribution



d) Shear stress distribution



e) Heat flux distribution

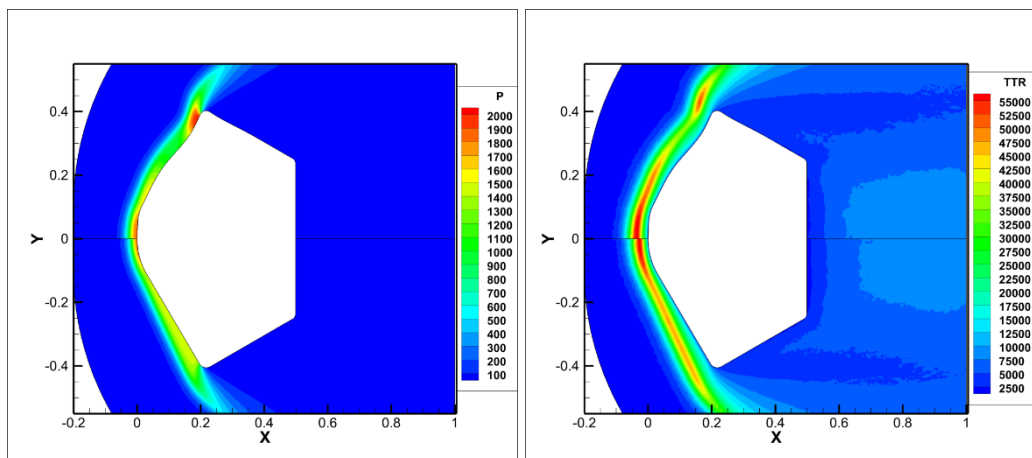
Figure 26 Comparison of Stardust and Opt. geom. 2

Table 8 Tabulated results of Stardust and Opt. geom. 2

<i>GEOMETRY</i>	<i>PRES. FORCE(N)</i>	<i>SHEAR FORCE(N)</i>	<i>TOT. DRAG FORCE(N) CONST.</i>	<i>MAX. HEAT FLUX(W/m²) CONST.</i>	<i>TOT. HEAT ENERGY(W) OBJ. FUNC. (min.)</i>	<i>VOLUME (m³) CONST.</i>
STARDUST	727.94	48.29	776.22	4308100	1373604	0.14519
OPT.GEOM.2	738.43	37.75	776.19	4316500	1245550	0.14561

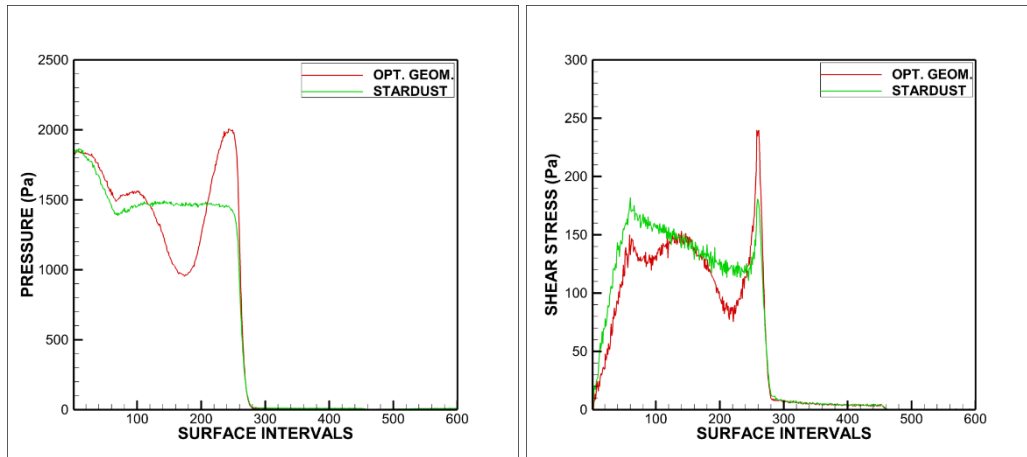
In the second optimization case, the objective function was changed to minimization of total heating energy while constraining the drag, maximum heat flux and volume. At the end of the optimization, Opt. geom. 2 was found. Total drag force, maximum heat flux value and volume were preserved, total heating energy was decreased.

Similar to Opt. geom. 1, wavy surface was obtained. Therefore, the distribution graphs were obtained as similar to Opt. geom. 1's (Fig. 25-26 c, d and e). However, the concavity of the Opt. geom. 2's surface near shoulder region is slighter than Opt. geom. 1's. This causes lower pressure values over there (Fig. 26 a), in other words the red region disappears (Fig. 25-26 a). So, the resulting drag force is not as high as the Opt. geom. 1's (Table 7 and Table 8). Besides, Opt. geom. 2's blunt nose height is shorter than Opt. geom. 1's. Thus, the thermal shock core cannot be pushed further that much (Fig. 25 b and Fig. 26 b). Therefore, the maximum heat flux value is not reduced as much as it is in Opt. geom. 1 (Table 7 and 8).



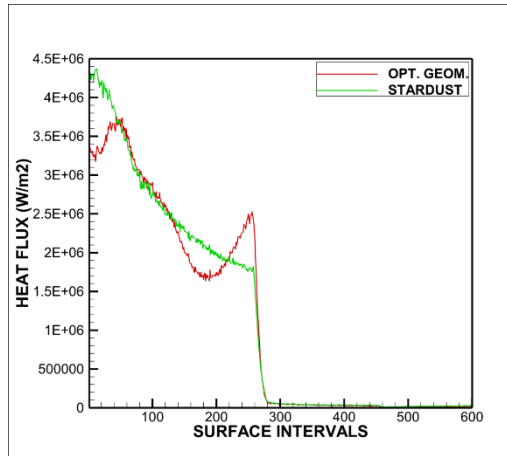
a) Pressure contours

b) Translational temperature contours



c) Pressure distribution

d) Shear stress distribution



e) Heat flux distribution

Figure 27 Comparison of Stardust and Opt. geom. 3

Table 9 Tabulated results of Stardust and Opt. geom. 3

<i>GEOMETRY</i>	<i>PRES. FORCE(N)</i>	<i>SHEAR FORCE(N)</i>	<i>TOT. DRAG FORCE(N) CONST.</i>	<i>MAX. HEAT FLUX(W/m²) OBJ. FUNC. (min.)</i>	<i>TOT. HEAT ENERGY(W) CONST.</i>	<i>VOLUME (m³) CONST.</i>
STARDUST	727.94	48.29	776.22	4308100	1373604	0.14519
OPT.GEOM.3	719.18	47.19	766.37	3680700	1358001	0.14532

In the third case, the objective function was changed to minimization of maximum heat flux. The total drag, heating energy and volume was constrained to the values of Stardust. At the end of the optimization, Opt. geom. 3 was found. Total heating energy and volume were preserved, and maximum heat flux value was decreased. Total drag was also supposed to be preserved but it decreased a bit. According to

the POD-RBF result, it was preserved (Table 5 and Table 9). However, an acceptable disagreement was found between DS2V and POD-RBF results.

Being different than the other two cases, optimized geometry was found in convex form except the region close to shoulder. By the effect of dominant convexity, the thermal shock core is pushed further significantly (Fig. 27 b). Thus, significant decrement can be achieved in maximum heat flux value (Table 9). At the same time, convexity also decreases the pressure as stated before, however this decrement is balanced with concavity which is close to shoulder region (Fig. 27 a).

The similarity of the pressure and shear stress distributions (Fig. 27 c and d) between Opt. geom. 3 and Stardust, are the result of having similar nose regions (Fig. 27 a). Supportively, pressure and shear distribution plots show the same trend up to 100th interval (Fig. 27 c and d). They both have blunt noses and have flatty regions after turning the corner. The flatty region similarity can also be seen from heat flux plot (Fig. 27 e) between 50th and 150th intervals. The difference up to 50th interval is sourced by the relatively blunter nose of Opt. geom. 3.

CHAPTER 7

CONCLUSION

In this study, two dimensional aerothermodynamic shape optimization study were conducted on Stardust reentry in near continuum regime. One of the trajectory points was chosen and axisymmetric calculations were conducted. Design of experiment was designated arbitrarily and developed step by step. Cubic B-spline curves were utilized in the geometry parameterization innovatively. Thus, the number of design variables was able to be reduced, and curve fitting cancelled. Two dimensional axisymmetric DSMC solver DS2V was utilized as the physics solver, and flow variable distribution (pressure, shear stress and heat flux) results along the geometry, were implemented in the POD-RBF network. In this manner, success of POD-RBF network was investigated on hypersonic flow conditions.

Extrapolation capability of the method was found as successful and can provide almost excellent agreement with the simulation results if the prospective geometry is in the scope of the snapshot pool. Despite arbitrarily sampled snapshot pool, the method's extrapolation accuracy shows that it is an appropriate method while reducing the orders of highly nonlinear hypersonic flows. The extrapolation accuracy can be developed further by means of sampling methods (e.g. Latin Hypercube sampling) while forming the design of experiment and it may be the subject of the future works.

POD-RBF network was used as the solver of the optimization; thus, it provides efficient reduction in the optimization time. Noting that, while any of DSMC solution requires at least 4 hours of computation time on an intel core i7-6700 HQ CPU 2.60 GHz, any response solution vector can be obtained in seconds by ROM.

Besides, although the solution pool of the ROM requires a considerable amount of time to simulate the all of 90 different geometries that compose the design of experiment, once this pool is obtained, the POD-RBF network provides response solutions by means of linear algebra. This makes possible to reduce the optimization time. In addition to this, since the solution pool is composed of high fidelity solutions of different geometries, they may be used for different purposes for the future studies.

REFERENCES

- [1] G. A. Bird, *Molecular Gas Dynamics and the Direct Simulation of Gas Flows*. Oxford: Oxford University Press, 1994.
- [2] A. L. Garcia, “Direct Simulation Monte Carlo : Theory, Methods, and Open Challenges,” Berkeley, RTO-EN-AVT-194, 2011.
- [3] Y.-L. He and W.-Q. Tao, “Multiscale Simulations of Heat Transfer and Fluid Flow Problems,” *J. Heat Transfer*, vol. 134, no. 3, p. 031018, 2012.
- [4] G. A. Bird, *The DSMC Method*. Sydney: CreateSpace, an Amazon company, 2013.
- [5] W. H. A. Schilders, H. A. van der Vorst, and J. Rommes, *Model Order Reduction: Theory, Research Aspects and Applications*. Berlin: Springer-Verlag, 2008.
- [6] A. I. Moreno, A. A. Jarzabek, J. M. Perales, and J. M. Vega, “Aerodynamic database error filtering via high order singular value decomposition,” *Aerosp. Sci. Technol.*, vol. 52, pp. 115–128, 2016.
- [7] T. Bui-Thanh, M. Damodaran, and K. E. Willcox, “Aerodynamic Data Reconstruction and Inverse Design Using Proper Orthogonal Decomposition,” *AIAA J.*, vol. 42, no. 8, pp. 1505–1516, 2004.
- [8] T. Bui-Thanh, M. Damodaran, and K. Willcox, “Proper Orthogonal Decomposition Extensions for Parametric Applications in Compressible Aerodynamics,” in *21st AIAA Applied Aerodynamics Conference*, 2003, pp. 1–11.
- [9] T. Sevine, “Reconstruction of Atmospheric Flows Based on Proper Orthogonal Decomposition Method,” Middle East Technical University, 2017.
- [10] J. Li and W. Zhang, “The performance of proper orthogonal decomposition in discontinuous flows,” *Theor. Appl. Mech. Lett.*, vol. 6, no. 5, pp. 236–

- 243, 2016.
- [11] J. Luo, “Design optimization of the last stage of a 4.5-stage compressor using a POD-based hybrid model,” *Aerosp. Sci. Technol.*, vol. 76, pp. 303–314, 2018.
 - [12] J. Q. Luo, Y. L. Zhu, X. Tang, and F. Liu, “Flow reconstructions and aerodynamic shape optimization of turbomachinery blades by POD-based hybrid models,” *Sci. China Technol. Sci.*, vol. 60, no. 11, pp. 1658–1673, 2017.
 - [13] S. Walton, O. Hassan, and K. Morgan, “Reduced order modelling for unsteady fluid flow using proper orthogonal decomposition and radial basis functions,” *Appl. Math. Model.*, vol. 37, no. 20–21, pp. 8930–8945, 2013.
 - [14] X. Chen, L. Liu, T. Long, and Z. Yue, “A reduced order aerothermodynamic modeling framework for hypersonic vehicles based on surrogate and POD,” *Chinese J. Aeronaut.*, vol. 28, no. 5, pp. 1328–1342, 2015.
 - [15] C. A. Rogers, A. J. Kassab, E. A. Divo, Z. Ostrowski, and R. A. Bialecki, “An inverse POD-RBF network approach to parameter estimation in mechanics,” *Inverse Probl. Sci. Eng.*, vol. 20, no. 5, pp. 749–767, 2012.
 - [16] B. Benaissa, M. Köppen, M. Abdel Wahab, and S. Khatir, “Application of proper orthogonal decomposition and radial basis functions for crack size estimation using particle swarm optimization,” *J. Phys. Conf. Ser.*, vol. 842, no. 1, 2017.
 - [17] H. Kato and K. Funazaki, “POD-Driven Adaptive Sampling For Efficient Surrogate Modeling and Its Application to Supersonic Turbine Optimization,” in *Proceedings of ASME Turbo Expo 2014: Turbine Technical Conference and Exposition*, 2014, pp. 1–10.
 - [18] V. R. Inc., “DOT Optimization.” [Online]. Available: <http://www.vrand.com/products/dot-optimization/>.

- [19] G. N. Vanderplaats and S. R. Hansen, *DOT Users Manual*. VMA Engineering, 1990.
- [20] A. J. Lofthouse, “Nonequilibrium Hypersonic Aerothermodynamics Using the Direct Simulation Monte Carlo and Navier-Stokes Models,” The University of Michigan, 2008.
- [21] N. Şengil, “Mikro Gaz Akışlarının DSMC (Doğrudan Benzetim Monte Carlo) Yöntemi ile Çözülmesi,” İstanbul Technical University, 2008.
- [22] D. Dirx and E. Mooij, *Conceptual Shape Optimization of Entry Vehicles: Applied to Capsules and Winged Fuselage Vehicles*. Switzerland: Springer International Publishing, 2017.
- [23] D. F. Rogers and J. A. Adams, *Mathematical Elements for Computer Graphics*, 2nd editio. McGraw-Hill, 1990.
- [24] I. D. Boyd, K. A. Trumble, and M. J. Wright, “Modeling of Stardust Entry at High Altitude, Part 1: Flowfield Analysis,” *J. Spacecr. Rockets*, vol. 47, no. 5, pp. 708–717, 2010.
- [25] L. Sirovich and M. Kirby, “Low-Dimensional Procedure for the Characterization of Human Faces,” *J. Opt. Soc. Am. A*, vol. 4, pp. 519–524, 1987.
- [26] L. Sirovich, “Turbulence and the Dynamics of Coherent Structures, I-III,” *Q. Appl. Math.*, vol. 45, no. 3, pp. 561–571, 1987.
- [27] R. D. Dony, “Karhunen-Loeve Transform,” in *The Transform and Data Compression Handbook*, CRC Press LLC, 2001.
- [28] L. I. Smith, “A Tutorial on Principal Components Analysis Introduction,” 2002.
- [29] M. Toyer, “Radial Basis Functions,” 2012.
- [30] G. N. Vanderplaats, “Basic Concepts,” in *Multidiscipline Design Optimization*, Vanderplaats Research & Development Inc.

- [31] G. A. Bird, "Nonequilibrium radiation during re-entry at 10 km/s," in *AIAA 22nd Thermophysics Conference*, 1987.